Global upper-mantle structure from finite-frequency surface-wave tomography

Ying Zhou,[1,2] Guust Nolet,[1] F. A. Dahlen,[1] and Gabi Laske[3]

[1]   We report global shear-wave velocity structure and radial anisotropy in the upper mantle obtained using finite-frequency surface-wave tomography, based upon complete three-dimensional Born sensitivity kernels. Because wavefront healing effects are properly taken into account, finite-frequency surface-wave tomography improves the resolution of small-scale mantle heterogeneities, especially for deep anomalies that are constrained by the longest-period surface waves. In our finite-frequency model FFSW1, the globally averaged radial anisotropy shows a transition from positive (SH > SV) to negative anisotropy (SV > SH) at about 220 km, consistent with a change in the dominant mantle circulation pattern from predominantly horizontal flow at shallow depths to vertical flow at greater depths. The radial anisotropy beneath cratons and the old Pacific plate agrees well with previous studies. However, our model exhibits a strong negative radial anisotropy at depths greater than 120 km beneath mid-ocean ridges, a feature that is not present in previous upper-mantle models. More interestingly, the depth extent of the ridge anomalies is distinctly different beneath fast- and slow-spreading centers; anomalies beneath fast-spreading centers are stronger, but the strength decreases rapidly below 250 km. In contrast, beneath slow-spreading centers such as the northern Mid-Atlantic Ridge and the Red Sea, anomalies extend down at least to the top of the transition zone. The different depth extent of the ridge anomalies suggests that the primary driving force of slow-spreading seafloor may be different from that of fast-spreading seafloor and that active upwelling beneath slow-spreading ridges may play a major role in the opening of the seafloor.

Citation: Zhou, Y., G. Nolet, F. A. Dahlen, and G. Laske (2006), Global upper-mantle structure from finite-frequency surface-wave tomography, *J. Geophys. Res.*, *111*, B04304, doi:10.1029/2005JB003677.

1.   Introduction

[2]   Radial anisotropy, meaning that horizontally polarized shear waves (SH waves) travel faster ($\beta_H > \beta_V$) or slower ($\beta_H < \beta_V$) than vertically polarized shear waves (SV waves), has been documented in long-period surface waves since the early 1960s [e.g., *Anderson*, 1961; *Aki and Kaminuma*, 1963]. It is now well accepted that an isotropic upper mantle can not explain both Love wave and Rayleigh wave dispersions. *Dziewonski and Anderson* [1981] incorporated a globally averaged radial anisotropy in the uppermost 220 km of their Preliminary Reference Earth Model (PREM). *Nataf et al.* [1984] first mapped three-dimensional global radial anisotropy down to 450 km depth, using long-period Love and Rayleigh dispersion curves expanded to spherical harmonic degree six. The origin of radial anisotropy in the upper mantle is not yet well understood, but it is usually presumed to be a result of the lattice preferred orientation (LPO) of mantle anisotropic minerals such as olivine, orthopyroxene, and clinopyroxene. LPO-induced mantle radial anisotropy is generally considered to be an indication of predominantly vertical or horizontal mantle flow.

[3]   Lateral variations of shear-wave velocity and radial anisotropy in the upper mantle have been studied by several research groups using ray-theoretical tomography [e.g., *Zhang and Tanimoto*, 1992; *Su et al.*, 1992; *Ekström and Dziewonski*, 1998]. *Gung et al.* [2003] investigated upper-mantle anisotropy using two-dimensional coupled-mode waveform sensitivity kernels and concluded that strong radial anisotropy is present beneath most cratons. Shear-wave velocity and anisotropy structures obtained by ray-theoretical tomography are limited to low-resolution inversions because ray theory is a high-frequency approximation, which becomes invalid whenever the length scale of the heterogeneities is smaller than the width of the Fresnel zone. As a result, only relatively large-scale structures can be trusted in ray-theoretical tomographic models. In this paper, we invert a small phase-delay data set for upper mantle *S*-wave velocity structure and radial anisotropy based upon theoretically well-founded, three-dimensional, finite-frequency, surface-wave

[1]Department of Geosciences, Princeton University, Princeton, New Jersey, USA.
[2]Now at Seismological Laboratory, California Institute of Technology, Pasadena, California, USA.
[3]Institute of Geophysics and Planetary Physics, Scripps Institution of Oceanography, University of California, San Diego, La Jolla, California, USA.

sensitivity kernels, computed in a background spherical Earth. In contrast to several other studies attempting to overcome the shortcomings of ray theory, the sensitivity kernels applied in our study fully account for the effects of directional scattering, source radiation, and the time-domain tapering used in making the dispersion measurements. *Zhou et al.* [2004] show that all these effects are important and should not be neglected. A detailed comparison between traditional ray-theoretical tomography and finite-frequency tomography has been presented in a companion paper [*Zhou et al.*, 2005].

[4] It is worth emphasizing again that the resolution in finite-frequency tomography is no longer limited by the high-frequency approximation that is inherent in ray theory; therefore it is possible to resolve smaller-scale mantle heterogeneities even with a small data set limited to long-period surface waves. In practice, finite-frequency tomography fits surface-wave dispersion data better than traditional ray theory [*Zhou et al.*, 2005].

[5] In this first application of our finite-frequency surface-wave theory, we invert the fundamental-mode Love and Rayleigh wave phase-delay measurements of *Laske and Masters* [1996]. Because Love waves are mostly sensitive to SH velocity, whereas Rayleigh waves are mostly sensitive to SV velocity, separate inversions of Love waves and Rayleigh waves provide insight into radial anisotropy in the upper mantle. In our model, strong fast anomalies are present beneath continental cratons, extending to about 250 km depth in both the SH and SV models, with anomalies diminishing in strength below 330 km. The continental cratons as well as the old Pacific plate are characterized by strong positive anisotropy ($\beta_H > \beta_V$), in good agreement with previous studies [e.g., *Ekström and Dziewonski*, 1998; *Gung et al.*, 2003]. Mid-ocean ridge anomalies are characterized by strong negative radial anisotropy below 120 km. At fast spreading centers, ridge anomalies are strong and mostly confined to the uppermost 250 km, However, at slow-spreading centers such as the northern Mid-Atlantic Ridge and the Red Sea, some ridge anomalies extend down at least to the top of the transition zone. We suggest that the driving force associated with slow-spreading seafloor may be fundamentally different from that associated with fast-spreading seafloor; active upwelling beneath slow-spreading ridges may play a major role in the initial opening of the sea floor.

2. Theoretical Background

2.1. Finite-Frequency Tomography

[6] Seismic waves have finite frequencies. Whenever the velocities of the medium vary only smoothly over space so that the characteristic length scale of the anomalies is much larger than the seismic wavelength of interest, wave propagation can be approximated by ray perturbation theory, a high-frequency approximation. The advantage of ray perturbation theory is its simplicity; however, it breaks down whenever the size of heterogeneities becomes too small so that wavefront healing and other finite-frequency effects that are ignored by ray theory are no longer negligible. As a result, the spatial resolution of ray theory in long-period surface-wave tomography is limited to large-scale structures. It is likely that deep features are even less reliable in ray-theoret-

ical surface-wave tomography, since deep anomalies are mainly constrained by surface waves of long period.

[7] In this paper we formulate the tomographic problem based upon the finite-frequency theory of *Zhou et al.* [2004], in which a measured surface-wave phase delay $\delta\phi$ is written as a linear volumetric integration over heterogeneities of shear-wave and compressional-wave speed perturbations ($\delta\beta/\beta$ and $\delta\alpha/\alpha$) in the three-dimensional Earth $\oplus$:

$$\delta\phi(\omega) = \iiint_\oplus K_\beta(\omega, \mathbf{x}) \frac{\delta\beta}{\beta}(\mathbf{x}) d^3\mathbf{x}, \qquad \text{Love waves,} \qquad (1)$$

$$\delta\phi(\omega) = \iiint_\oplus \left[K_\beta(\omega, \mathbf{x}) \frac{\delta\beta}{\beta}(\mathbf{x}) + K_\alpha(\omega, \mathbf{x}) \frac{\delta\alpha}{\alpha}(\mathbf{x}) \right] d^3\mathbf{x}, \qquad (2)$$

Rayleigh waves.

In equations (1) and (2), the quantity ω is the angular frequency of surface waves, and the integration kernels, K_β and K_α represent the sensitivity of a phase delay to lateral perturbations in the shear-wave speed (β_H or β_V) and compression-wave speed (α), respectively. The effects of density perturbations have been ignored for simplicity, based on the following considerations: (1) if we assume mantle anomalies are dominantly thermal, velocity variations are much more significant than density variations; and (2) fundamental-mode surface-wave phase delays are most sensitive to velocity perturbations [*Zhou et al.*, 2004]. The sensitivity kernels are formulated based on the first-order Born approximation in a background spherical Earth, which fully takes into account the effects of directional scattering, seismic source radiation, and the tapering applied to the seismogram in making the phase-delay measurements. The effects of surface-wave cross-branch model-coupling are ignored in this study because the number of measurements affected by significant surface-wave mode coupling is likely to be small in our hand-picked data set, and our previous study suggests that the effects of mode-coupling is not significant for the spatial resolution considered in this global study [*Zhou et al.*, 2004]. We compute the fundamental-mode three-dimensional (3-D) Born sensitivity kernels K_β and K_α without making any simplifications in the computation (e.g., forward scattering or forward propagation). The features of 3-D sensitivity kernels have been discussed by *Zhou et al.* [2004]; examples of the kernels K_β and K_α for 10 mHz Love wave and Rayleigh wave are plotted in Figure 1, for the spherically symmetric reference Earth model, 1066A [*Gilbert and Dziewonski*, 1975]. Figure 1 shows that Love waves have no sensitivity to perturbations in the compressional-wave speed (i.e., $K_\alpha = 0$); Rayleigh waves have some sensitivity to the compressional wave speed at shallow depths. In general, surface-wave sensitivities are concentrated in a broad region around the great-circle ray, and the sensitivity is neither maximum nor zero along the great-circle ray. The width of the sensitivity kernels increases with the period of the seismic wave; the geometry of the kernels also depends upon the epicentral distance, the radiation pattern of the seismic source, and the wave trains of interest (Figure 2).

[8] The limitation of spherical-earth Born sensitivity kernels in global mantle tomography are not well under-

(a) Love wave K_β (b) Rayleigh wave K_β (c) Rayleigh wave K_α
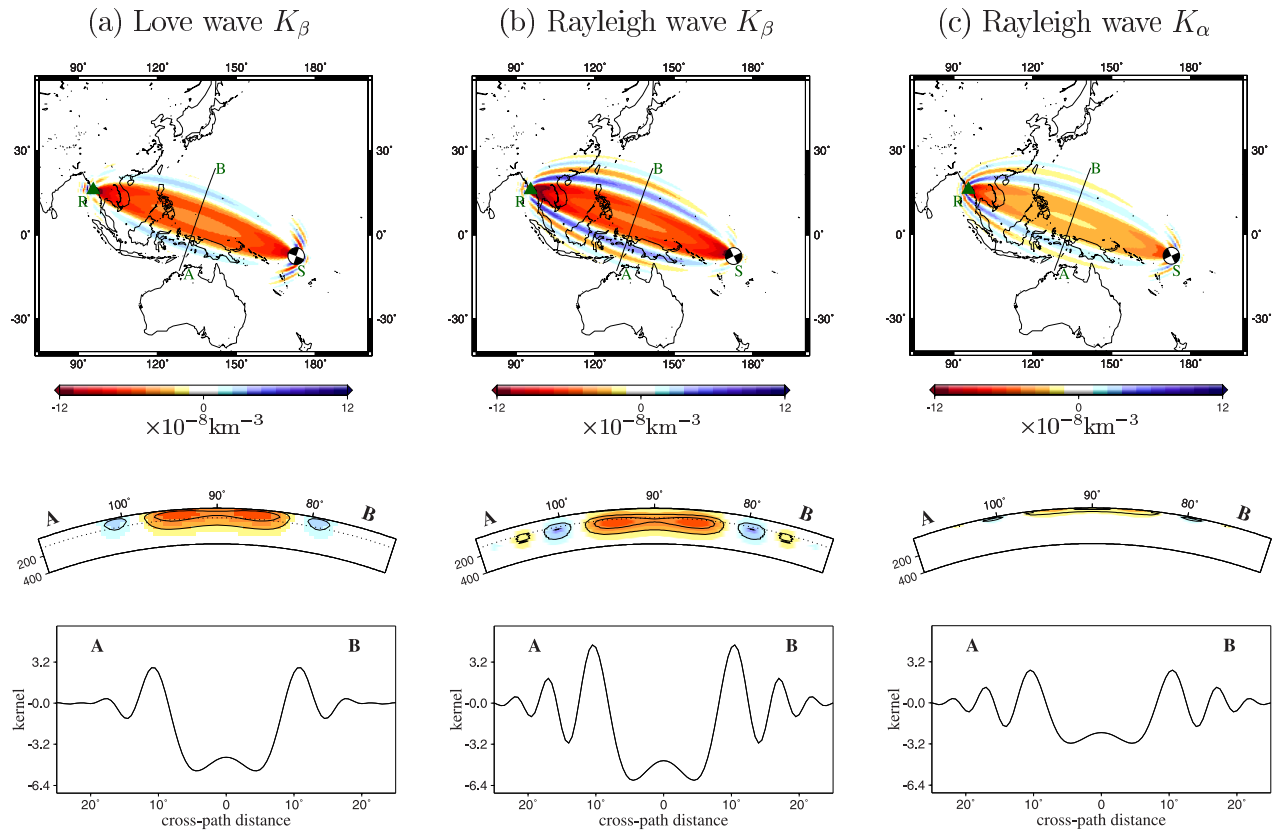
Figure 1. (a) The 10-mHz Love-wave phase-delay sensitivity kernel K_β, expressing the sensitivity to shear-wave velocity perturbations $\delta\beta/\beta$. (b) and (c) Rayleigh wave phase-delay sensitivity kernels K_β and K_α (the latter expressing sensitivity to compressional wave speed perturbations $\delta\alpha/\alpha$). Top three plots show map views at a depth of 108 km; middle three plots show vertical slices along AB across-section with 108 km depth indicated by dotted lines; bottom three plots show AB cross-path variations in sensitivity at 108 km depth. The seismic sources are vertical strike-slip (beach balls), with maximal radiation along the great-circle ray. The sensitivity kernels are computed for a spherically symmetric reference Earth model, 1066A [*Gilbert and Dziewonski*, 1975].

stood. If mantle velocity perturbations are small with respect to model 1066A, we expect the Born sensitivity kernels used in this paper to be adequate for mantle tomography. In general, tomographic models can be further improved by iterating the reference Earth model. However, Born sensitivity kernels for a background, laterally heterogeneous reference Earth model require heavy computation [e.g., *Yoshizawa and Kennett*, 2005; *Zhao et al.*, 2005], and implementing 3-D reference Born sensitivity kernels in global tomography is still a computational challenge.

2.2. Radial Anisotropy

[9] In weakly anisotropic media, surface-wave phase velocities (*c*) can be completely described in terms of thirteen combinations of elastic coefficients, with five parameters *A*, *C*, *F*, *L*, and *N* describing radial anisotropy [*Love*, 1927]. Radial anisotropy has a vertical axis of symmetry, and the resulting phase velocity is independent of the propagation azimuth θ; the other eight parameters account for the 2θ and 4θ azimuthal dependence [*Smith and Dahlen*, 1973; *Montagner and Nataf*, 1986]. On the basis of mineralogical and petrological models of the upper mantle, the parameters describing radial anisotropy are strongly correlated [*Montagner and Anderson*, 1989], and the best

resolvable parameters are the velocities of vertically and horizontally polarized shear waves, $\beta_V = \sqrt{L/\rho}$ and $\beta_H = \sqrt{N/\rho}$ [*Montagner and Nataf*, 1986]. To reduce the number of free parameters in the inversion, in view of the small number of phase delays in our data set, we vary only these two velocity parameters, β_V and β_H. Fundamental-mode Rayleigh waves have some sensitivity to the compressional-wave speed at shallow depth (Figure 1); to account for this, we scale the perturbation in compressional-wave speed to shear-wave speed perturbation using the relation

$$\delta \ln \alpha = f \delta \ln \beta_V, \tag{3}$$

adapted from lab measurements [*Montagner and Anderson*, 1989]. The scaling parameter *f* is chosen to be 0.5 in the inversion. We have experimented with values in the range $0 < f < 1$, and found the differences in resulting tomographic images are negligible at the depths of interest.

[10] Radial anisotropy can be regarded as the azimuthally averaged anisotropy of the upper mantle. The azimuthal dependence of anisotropy has been investigated at both the global and regional scale [e.g., *Forsyth*, 1975; *Tanimoto and Anderson*, 1985; *Montagner and Tanimoto*, 1990; *Debayle*
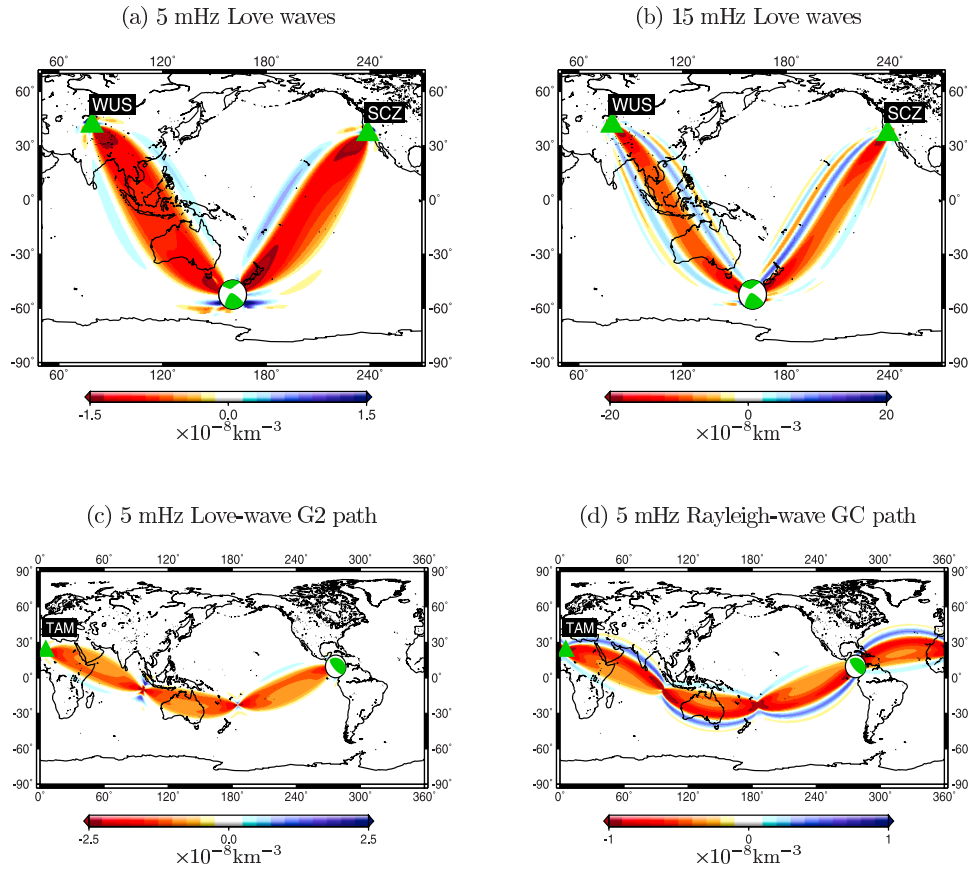
Figure 2. Example map views of three-dimensional (3-D) phase-delay sensitivity kernels K_β for the global data set of this study, plotted at a depth of 70 km. The sensitivity kernels are computed for a spherically symmetric reference Earth model, 1066A [*Gilbert and Dziewonski*, 1975]. (a) and (b) Sensitivity kernels for 5 mHz and 15 mHz minor-arc Love waves; the epicentral distances of the two seismic stations are 111.49° (SCZ) and 116.66° (WUS), respectively. (c) and (d) Sensitivity kernels for a Love-wave major arc (G2) and Rayleigh-wave great circle path (R3-R1) at a frequency of 5 mHz, respectively. The epicentral distance of station TAM is 85°. The source mechanisms are indicated by the green beach balls. The geometries of the sensitivity kernels are affected by the source radiation pattern and seismic frequency, as well as the wave train of measurement.

and Kennett, 2000; *Simons et al.*, 2002]. An important indication of the presence of azimuthal anisotropy is elliptical particle motion of quasi-Love waves [e.g., *Crampin*, 1975; *Tanimoto*, 2004]. In the dispersion data used in this study, elliptical Love-wave particle motions are observed at a few stations; however, the bulk of our observations are not consistent with any systematic azimuthal anisotropy, even in regions in the Pacific Ocean where one might expect strongly azimuthal anisotropy [*Laske and Masters*, 1996]. Therefore we ignore the effects of azimuthal anisotropy in this study and focus only upon the radial anisotropy with a vertical axis of symmetry.

[11] In anisotropic media, Love waves and Rayleigh waves are coupled. However, this coupling is probably negligible between fundamental-mode Love and Rayleigh waves. The Fréchet depth sensitivity kernels $\delta c/\delta\beta_V$ and $\delta c/\delta\beta_H$ for 10-mHz Love and Rayleigh waves are plotted in Figure 3. Clearly, fundamental-mode Love waves are primarily sensitive to the horizontally polarized shear-wave speed β_H, with only a slight sensitivity to the vertically polarized shear-wave speed β_V. Rayleigh waves, on the other hand, are primarily sensitive to β_V, with very little

sensitivity to β_H. In this study, we ignore the coupling between fundamental-mode Love and Rayleigh waves and investigate radial anisotropy based upon separate inversions of Love waves and Rayleigh waves. We also ignore the effects of *P*-wave anisotropy and scale the isotropic *P*-wave velocity perturbations to the SV velocity perturbations using equation (3).

3. Data and Tomography

3.1. Data, Model Parametrization, and Crustal Correction

[12] We use fundamental-mode phase-delay measurements of minor-arc, major-arc, and multiorbit Love waves (G1, G2, G3, G4) and Rayleigh waves (R1, R2, R3, R4). This data set includes a total of ~12000 wave trains, including both Love waves and Rayleigh waves. The measurements are made at single frequencies from 5 mHz to 15 mHz at 1 mHz intervals, with a multitaper technique applied to reduce spectral leakage [*Laske and Masters*, 1996]. Seismic sources and receivers are plotted in Figure 4a. The Pacific is well sampled by minor-arc wave trains, while the global path
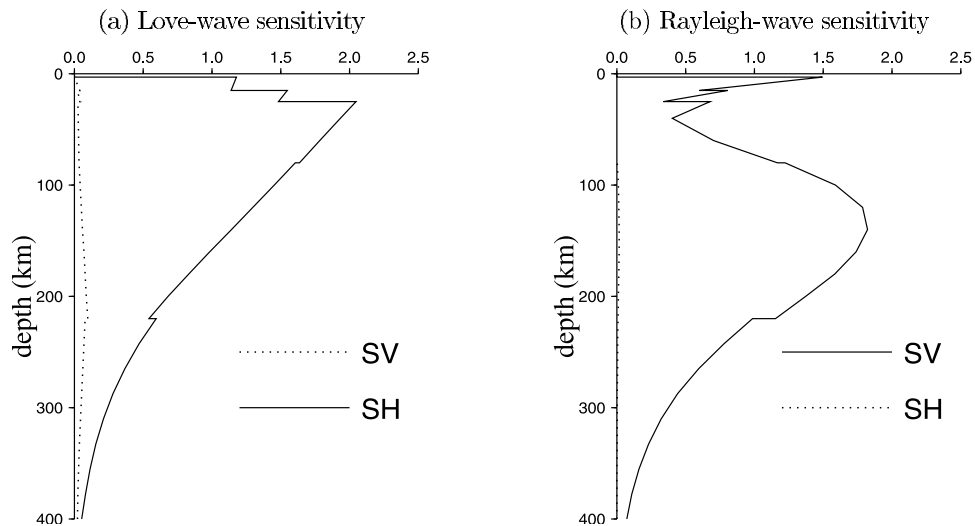
Figure 3. Sensitivity of fundamental-mode Love-wave and Rayleigh-wave phase velocity to perturbations in SV and SH velocities (β_V and β_H). The depth Fréchet kernels, $\delta c/\delta\beta_V$ and $\delta c/\delta\beta_H$ are computed for anisotropic Preliminary Reference Earth Model, PREM [*Dziewonski and Anderson*, 1981]. Love waves are primarily sensitive to perturbations in β_H and Rayleigh waves are primarily sensitive to perturbations in β_V.
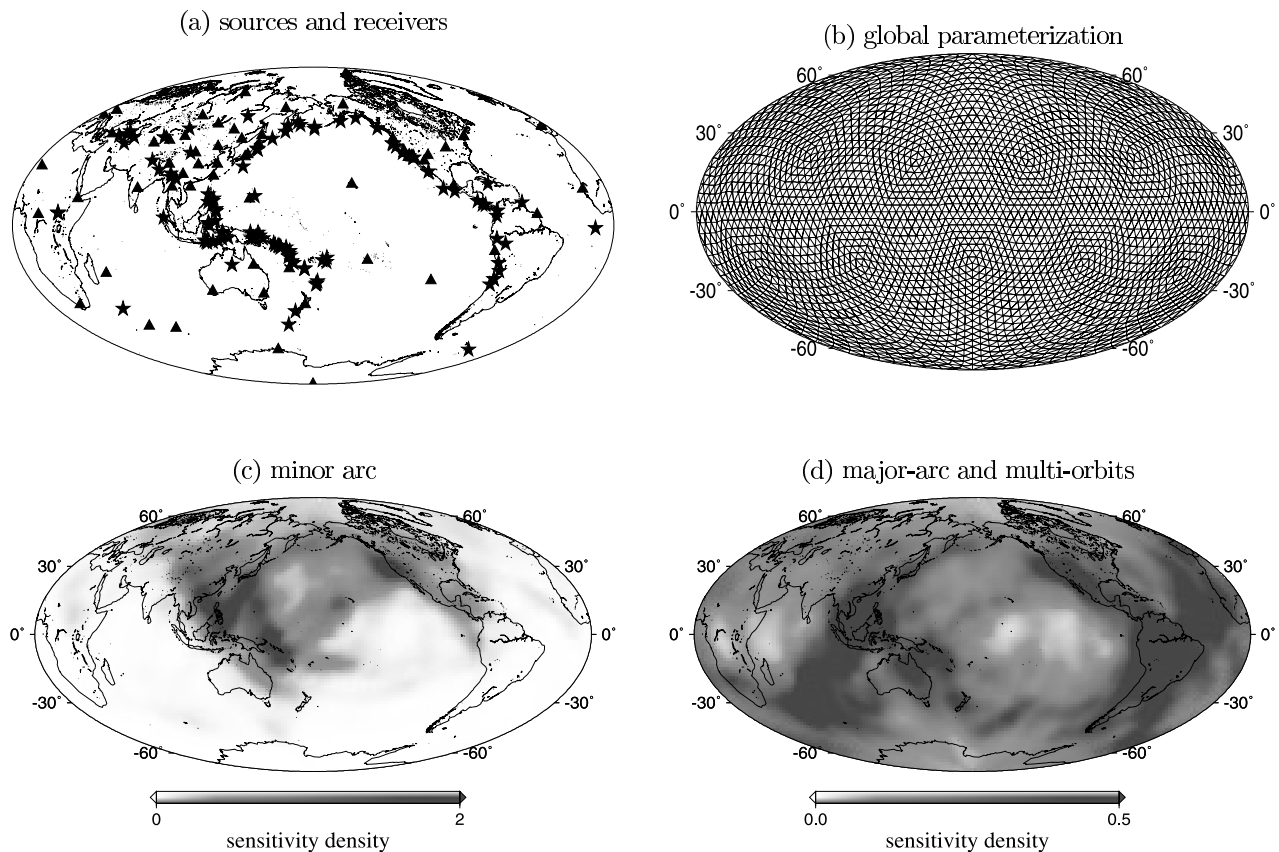
Figure 4. (a) Seismic sources (stars) and receivers (triangles) of the data set in this study. (b) The surface of the Earth is parameterized by a set of spherical triangular grid points [*Baumgardner and Frederickson*, 1985], with an average grid spacing of 4.3°. (c) Love-wave sensitivity density (the diagonal element of matrix A^TA) for minor arcs G1, plotted at a depth of 180 km. (d) Love-wave sensitivity density at 180 km, for wave trains including major arcs G2 and multi-orbits, G3 and G4.
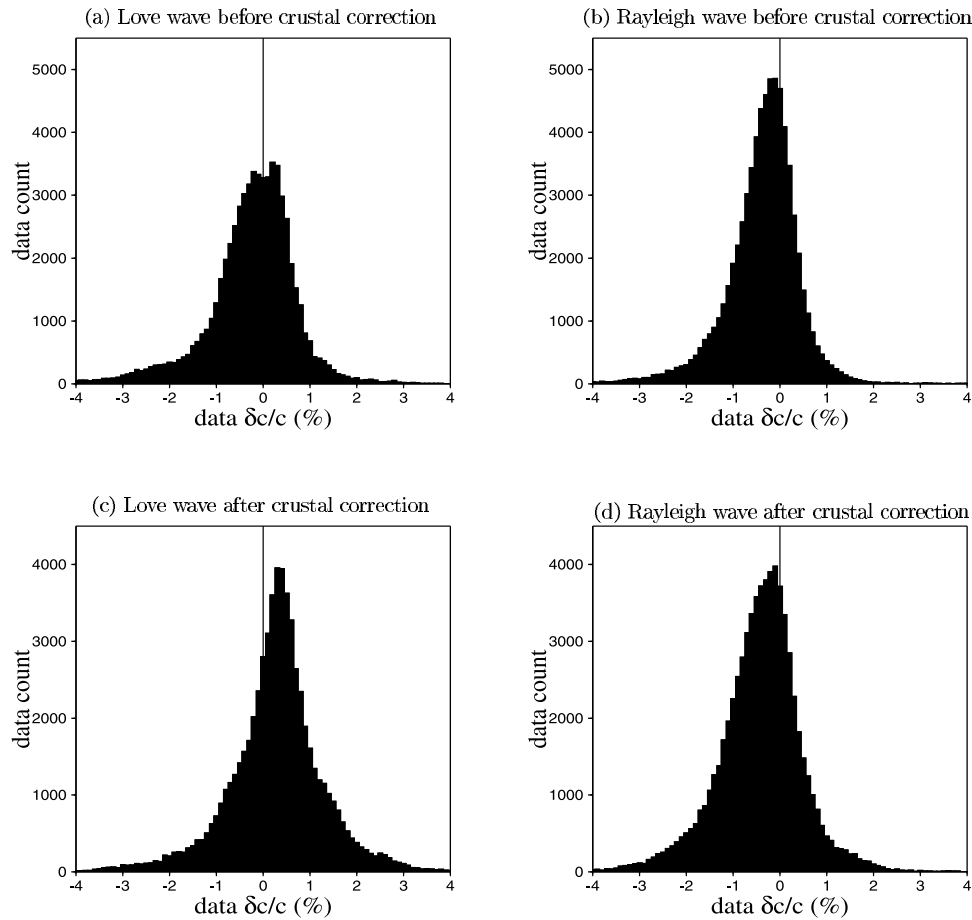
Figure 5. Histograms of Love and Rayleigh wave fractional phase-delay data ($\delta c/c = -\delta\phi/\phi$), including all frequencies from 5 mHz to 15 mHz. The residuals are with respect to a spherically symmetric reference Earth model, 1066A [*Gilbert and Dziewonski*, 1975]. Crustal corrections are based upon the global crustal model CRUST2.0 [*Laske et al.*, 2001]. Observed Love waves are in general faster than 1066A, whereas Rayleigh waves are slower than 1066A in this frequency range. The discrepancy between Love waves and Rayleigh waves is more significant after application of the crustal correction.

coverage is greatly improved by major-arc and multiorbit wave trains (Figures 4c and 4d). All phase-delay measurements are residuals with respect to synthetic seismograms computed for a spherically symmetric reference model, 1066A [*Gilbert and Dziewonski*, 1975]. As noted above, the kernels K_α and K_β reflect this; they describe the sensitivity away from as well as on the great-circle ray. Unreliable measurements in the hand-picked data set have been removed in the process of quality control. Ray-theoretical phase-velocity maps based on this phase-delay data set as well as on additional amplitude and polarization measurements have been published by *Laske and Masters* [1996]. We use only phase delays in this study because their interpretation is more reliable than that of amplitude and polarization data in the presence of strong heterogeneities. To reduce the effects of potential outliers, we exclude measurements that deviate more than three standard deviations from the value predicted by model 1066A. Uncertainties in seismic radiation may also introduce errors in finite-frequency tomography, especially for near-nodal stations, because the geometry of the finite-frequency sensitivity kernels is dependent upon the source radiation

pattern. We discard those measurements whose predicted surface-wave radiation in the direction of the reference ray is less than 10% of the maximum source radiation. Overall, this winnowing leaves about 95% of the original data set in the inversion.

[13] The surface of the Earth is parameterized into 2562 triangular grid points using the method of *Baumgardner and Frederickson* [1985]. The average spacing between neighborhood grid points is 4.3° (Figure 4b). The grid points are uniformly distributed and the standard deviation of the neighborhood grid spacing is about 0.3°. In the radial direction, the uppermost 580 km of the upper mantle is parameterized by nine grid points, with a nominal spacing of 60 km in the top 400 km.

[14] Surface waves are sensitive to crustal heterogeneities even at long period. Crustal signals in global surface-wave dispersion studies are usually removed by applying crustal corrections. It is not surprising that due to finite-frequency effects, surface waves are sensitive to Moho depth perturbations off the great-circle ray path. Those effects are not negligible and could be properly taken into account using finite-frequency sensitivity kernels in regional studies,
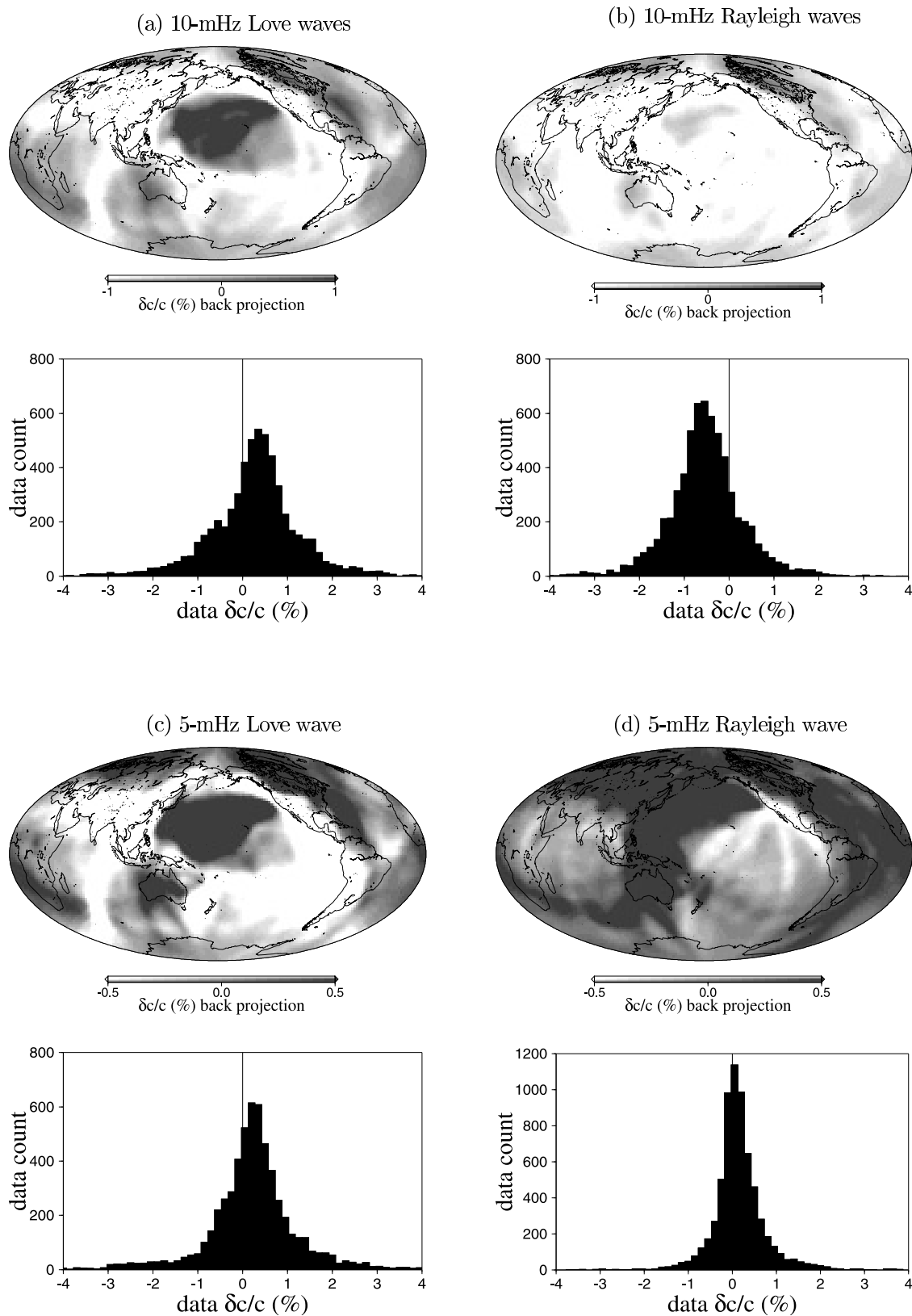
Figure 6. Discrepancy in the fractional phase delays ($\delta c/c = -\delta\phi/\phi$) between Love waves and Rayleigh waves at 10 mHz and 5 mHz. The residuals are with respect to a spherically symmetric reference Earth model, 1066A [*Gilbert and Dziewonski*, 1975]. (a) Back projection and data histogram for 10-mHz Love waves; (b) the same for 10-mHz Rayleigh waves. (c) and (d) are plotted at 5 mHz. It is worth noticing that Rayleigh-wave back-projection maps show a polarity change from dominantly slower (white) than model 1066A at 10 mHz to dominantly faster (dark gray) at 5 mHz.
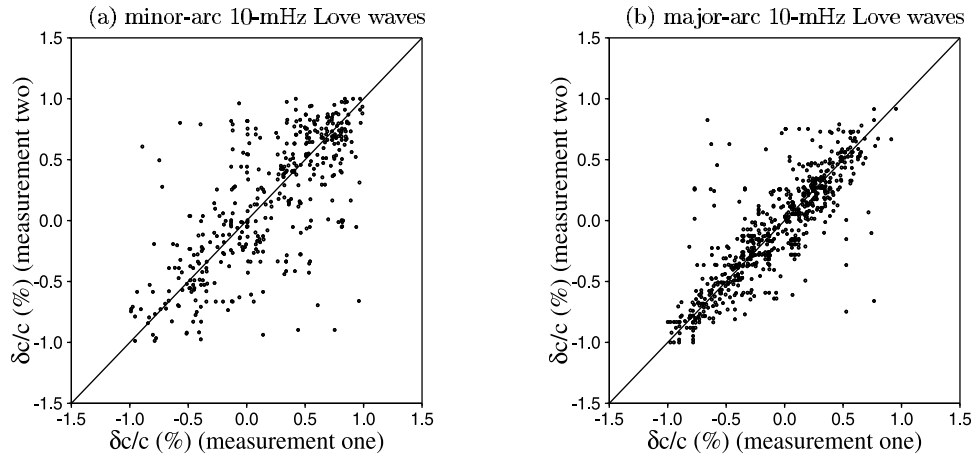
Figure 7. (a) Scatterplot of fractional phase-delay measurements ($\delta c/c = -\delta\phi/\phi$) made on repeating events, for 10-mHz minor-arc Love waves (G1). (b) Scatterplot for 10-mHz major-arc Love-wave (G2) measurements. Earthquake pairs that are less than 100 km apart in the long-period global surface-wave data set are treated as repeating events. The total number of event pairs is 915 for 10-mHz G1 paths and 751 for 10-mHz G2 paths, with good spatial coverage. The fractional noise RMS is estimated from the ratio of σ_n/σ_d, where $\sigma_d^2 = \langle(b - \bar{b})^2\rangle$ is the variance of the measurements made on those events; and $\sigma_n^2 = \langle(\delta b - \bar{\delta b})^2\rangle$ is the corresponding noise variance, with δb being the differential measurements between two repeating events. We have made the assumption that the measurements made on repeating earthquakes are correlated, which increases the noise variance by a factor of 2. The estimated fractional measurement errors are $\sigma_n/\sigma_d \approx 65\%$ in (a) 10-mHz G1 measurements, and $\sigma_n/\sigma_d \approx 45\%$ in (b) 10-mHz G2 measurements.

whenever the crustal thickness does not vary greatly [*Zhou et al.*, 2005]. However, in a global-scale study such as this, finite-frequency sensitive kernels for boundary perturbations may not be reliable for crustal corrections because finite-frequency sensitivity kernels are based upon linear perturbation theory and the variations in crustal thickness exceed the regime in which linear perturbation theory is valid [*Zhou et al.*, 2005]. In this study, we use ray theory for the crustal corrections and ignore the off-path contribution of Moho boundary perturbations. We correct the crustal signal based upon a global crustal model, CRUST2.0, which specifies a seven-layer crust in each 2° by 2° grid (available at http://mahi.ucsd.edu/Gabi/crust2.html). We compute Love and Rayleigh dispersion curves at each grid point using a local velocity model, adapted from the reference model 1066A and the seven-layer local crust. The histograms of the data, including all frequencies between 5 mHz and 15 mHz, are plotted in Figure 5 before and after crustal correction. The large crustal signal that is evident in Figure 5 confirms that a one-dimensional reference Earth model is far from sufficient for the crust and that crustal corrections are crucial in long-period surface wave investigations, as noted by many previous studies [e.g., *Dziewonski*, 1971; *Montagner and Jobert*, 1988].

3.2. Love-Rayleigh Discrepancy

[15] In Figure 5, Love wave and Rayleigh wave data show a distinct discrepancy. In general, Love waves are faster than predicted by model 1066A, whereas Rayleigh waves are slower than model 1066A, a possible indication of global radial anisotropy. This Love-Rayleigh discrepancy is more pronounced at high frequencies than at low fre-

quencies, and the geographic distribution of the discrepancy can be displayed if we back-project the fractional phase-delay data $\delta c/c = -\delta\phi/\phi$ using the formula

$$p(\hat{\mathbf{r}}, \omega) = \sum_{i=1}^{N} w_i(\hat{\mathbf{r}}) \frac{\delta c_i(\omega)}{c(\omega)}, \qquad (4)$$

where N is the total number of measurements, $\hat{\mathbf{r}}$ is the position vector on the unit sphere,

$$w_i(\hat{\mathbf{r}}) = \begin{cases} 1/\Delta & \hat{\mathbf{r}} \text{ on the } i\text{th ray path,} \\ 0 & \hat{\mathbf{r}} \text{ off the } i\text{th ray path.} \end{cases} \qquad (5)$$

is the back-projection weighting function for the ith fractional phase delay measurement $\delta c_i/c$, and $p(\hat{\mathbf{r}}, \omega)$ is the plotted data back-projection at frequency ω. In Figure 6, Love waves at 10 mHz exhibit faster phase velocities than model 1066A, whereas Rayleigh waves exhibit slower phase velocities than model 1066A. The back-projections of the 10-mHz phase-delay measurements display a strong discrepancy between Love and Rayleigh waves over the old Pacific. Love waves at 5 mHz remains faster than model 1066A, with a geographic distribution similar to that at 10 mHz. In contrast, Rayleigh waves at 5 mHz are slightly faster than model 1066A. The back-projection maps of Rayleigh-wave data show a polarity change, from dominantly slower (than 1066A) at 10 mHz to dominantly faster at 5 mHz. It is worth noting that data back-projections may be indicative of geographical localizations of anisotropy, but, since Love waves and Rayleigh waves have different depth sensitivities, a
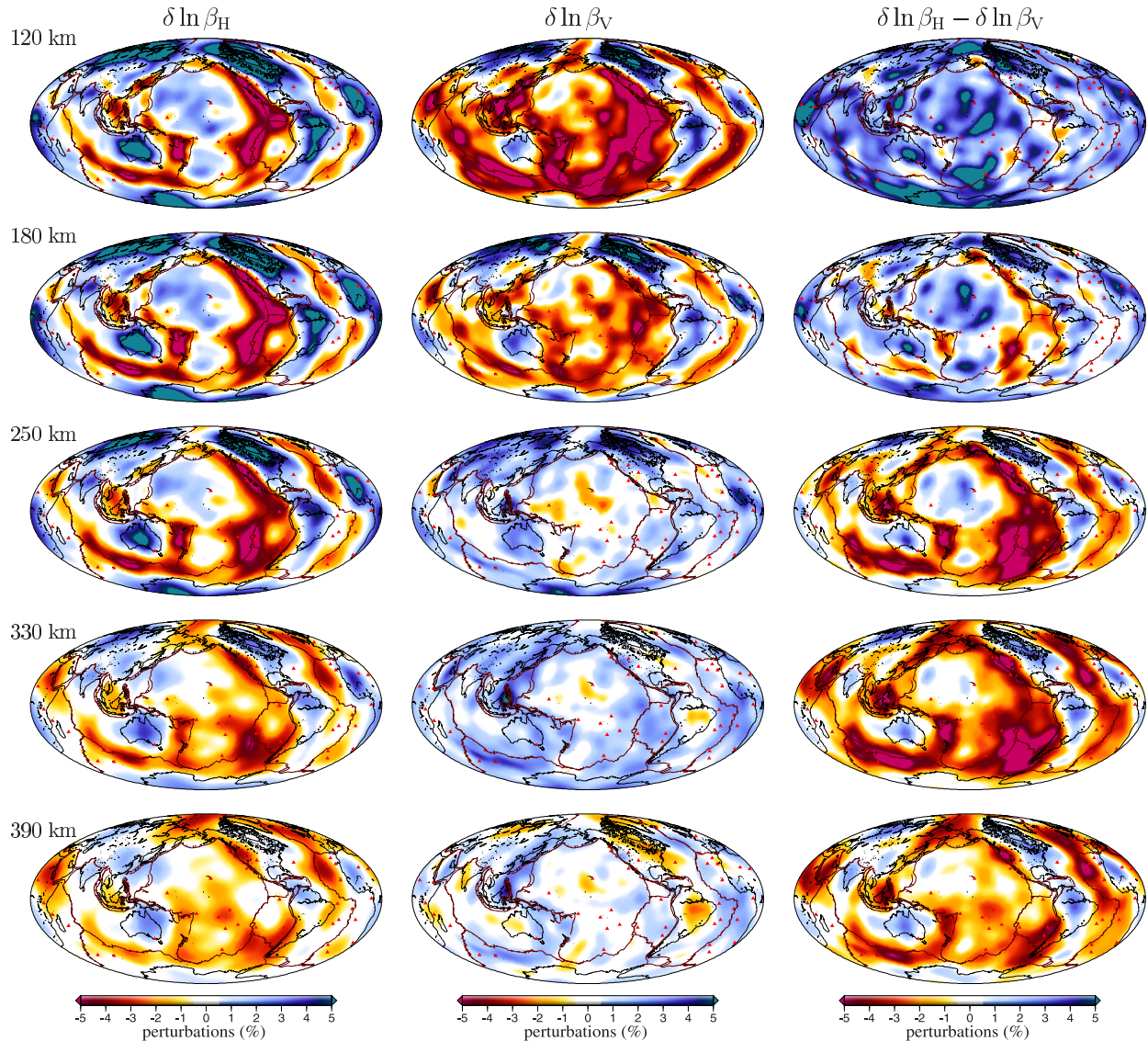
Figure 8. (a) Upper-mantle SH-wave velocity perturbations $\delta \ln \beta_H = \delta\beta_H/\beta_H$, plotted at the depths of 120 km, 180 km, 250 km and 390 km. (b) SV-wave velocity perturbations $\delta \ln \beta_V = \delta\beta_V/\beta_V$. (c) Radial anisotropy $\delta \ln \beta_H - \delta \ln \beta_V$. Velocity perturbations are with respect to a spherically symmetric reference Earth model, 1066A [*Gilbert and Dziewonski*, 1975]. Red triangles indicate locations of hot spots, and brown lines are plate boundaries.

careful interpretation of the anisotropy distribution must be made based upon our 3-D tomographic images (section 4).

3.3. Inversion Scheme

[16] We discretized the exact sensitivity kernels K_β and K_α in the volumetric integration (1) and (2), applying a dense spatial sampling to avoid possible aliasing. To limit the number of free parameters in the inversions, we assume that the velocity can be fully represented by a set of parameterized triangle grid points (Figure 4b) and that the velocity perturbations inside any triangle can be linearly interpolated using the triangle grid points. In the depth direction, velocity perturbations are interpolated linearly between neighboring grid points. Applying (3), the tomographic equation can be written in the canonical form

$$\mathbf{Am} = \mathbf{b}, \qquad (6)$$

where the element $\{A\}_{ij}$ in the matrix represents the sensitivity at the jth grid point for the ith phase-delay measurement, the jth element of the vector $\mathbf{m}$ represents the unknown parameter $\delta\beta_j/\beta_j$ at the jth grid point, and b_i represents the ith phase-delay measurement.

[17] The least squares solution to the inverse problem can be found from $(\mathbf{Am} - \mathbf{b})^T(\mathbf{Am} - \mathbf{b}) =$ minimum, where the superscript T indicates the transpose. The matrix $\mathbf{A}^T\mathbf{A}$ is a singular or ill-conditioned matrix in all practical seismic tomographic applications, leading to very large or infinite errors in the solution. We strike a balance between model resolution and model variance by introducing a trade-off parameter that regularizes the inverse problem. Two widely used regulation schemes are "smoothing" and "norm damping"; the smoothing approach sacrifices model roughness in return for reduced uncertainty of the resolved model by solving $(\mathbf{Am} - \mathbf{b})^T(\mathbf{Am} - \mathbf{b}) + \epsilon_s\|\mathbf{Sm}\| =$ minimum,
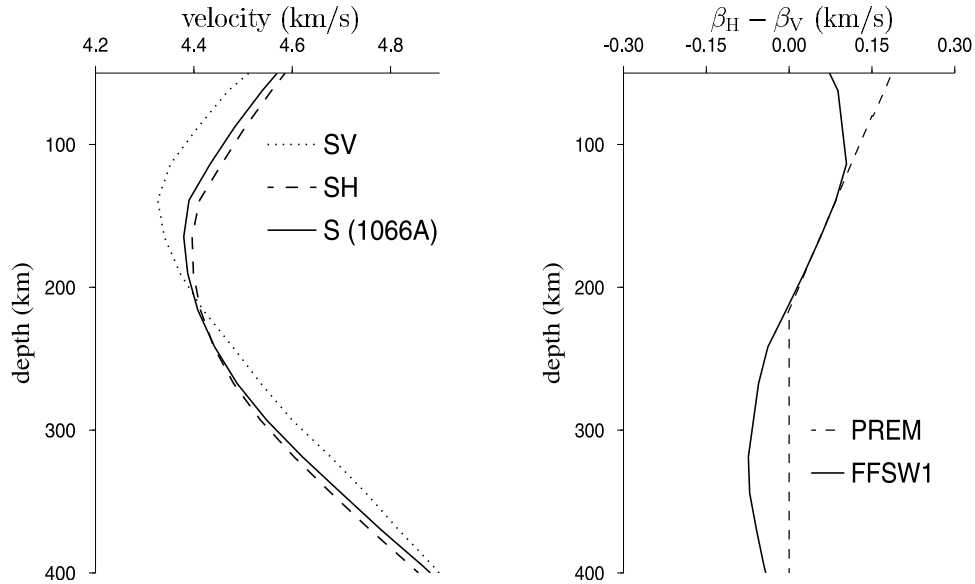
Figure 9. (left) Global average of radial anisotropy in model FFSW1. Vertically polarized shear waves (SV waves) are slower than horizontally polarized SH waves in the uppermost 220 km of the upper mantle (indicative of horizontal flow); SV waves become faster than SH waves below 220 km (indicative of vertical flow). (right) Comparison of radial anisotropy $\beta_H - \beta_V$ structure between PREM and model FFSW1. The finite-frequency tomographic model FFSW1 exhibits weaker radial anisotropy than PREM at depths shallower than 120 km, but it agrees with PREM at depths between 120 km and 220 km. PREM is isotropic below 220 km, whereas model FFSW1 shows negative radial anisotropy ($\beta_H < \beta_V$) below 220 km.

where $\|\mathbf{Sm}\|$ is a suitable roughness norm; norm damping is introduced into an inversion through $(\mathbf{Am} - \mathbf{b})^T(\mathbf{Am} - \mathbf{b}) + \epsilon_d \|\mathbf{m}\|^2$ = minimum, where ϵ_d governs the trade-off between model RMS and model accuracy. In this study, only smoothing is used to regularize the inversion; we minimize an approximate Laplacian by differencing every gridpoint with the average of its nearest neighbors, i.e., $\|\mathbf{Sx}\| \simeq \int \int \int |\nabla^2 (\delta\beta/\beta)| d^3\mathbf{x}$, where the integral is over the entire upper mantle.

[18] Phase-delay measurements are associated with observational errors such as bias in seismic spectrum estimates and uncertainties in source locations and seismic moment tensors. We estimate the observational errors from sets of closely located earthquakes in the data set. We expect surface waves generated by earthquake pairs that are less than 100 km apart to follow approximately the same propagation path and therefore to acquire very similar phase delays. The difference in phase delay between such repeating earthquakes provides a measure of the observational errors in a certain subset of the data. The scatterplots in Figure 7 illustrate our error estimates, 65% for 10-mHz minor-arc and 45% for major-arc Love waves, determined from repeating earthquake pairs. To be conservative, we assume that measurements made on repeating earthquakes are correlated, which increases the noise standard deviation by a factor of $\sqrt{2}$, compared to the standard deviation of entirely independent measurements. The number of earthquake pairs available in our data set is between 300 and 1000, depending upon wave train and frequency. The spatial coverage of the repeating paths is also reasonably good so that the statistics can be trusted.

[19] Using the standard deviation (σ) estimated from repeating earthquakes, the tomographic problem with

regulation based upon the model smoothness can be rewritten as

$$\chi^2 + \epsilon_s \| \mathbf{Sm} \|^2 = \text{minimum}, \quad \text{where} \quad \chi^2 = \sum_{i=1}^{N} \left(\frac{A_{ij}m_j - b_i}{\sigma_i} \right)^2, \tag{7}$$

where N is the total number of measurements, and summation over the model parameter index j in equation (7) is understood. In this study, we invert simultaneously for delays in event origin times, $\mathbf{t}$, with t_k being the delay time of the kth event. With this alteration, the tomographic equation solved in this study becomes

$$\chi^2 + \epsilon_s \| \mathbf{Sm} \|^2 + \epsilon_t \| \mathbf{t} \|^2 = \text{minimum},$$
$$\text{where} \quad \chi^2 = \sum_{i=1}^{N} \left(\frac{A_{ij}m_j + H_{ik}t_k - b_i}{\sigma_i} \right)^2, \tag{8}$$

where summation over the earthquake index k as well as the model parameter index j is now understood. The quantity $H_{ik}t_k$ represents the phase delay in the ith observation due to a shift in the origin time of the kth earthquake. We choose an origin-time damping parameter ϵ_t such that the perturbations t_k are not greater than ±4 s; because the surface waves used in this study are long-period (67–200 s), the differences between tomographic models inverted with and without origin-time corrections are negligible. The sparse linear tomographic problem (8) is solved using the LSQR algorithm [*Paige and Saunders*, 1982], iterated until full convergence. The smoothing parameter ϵ_s is chosen to make an optimal balance between the data misfit and model
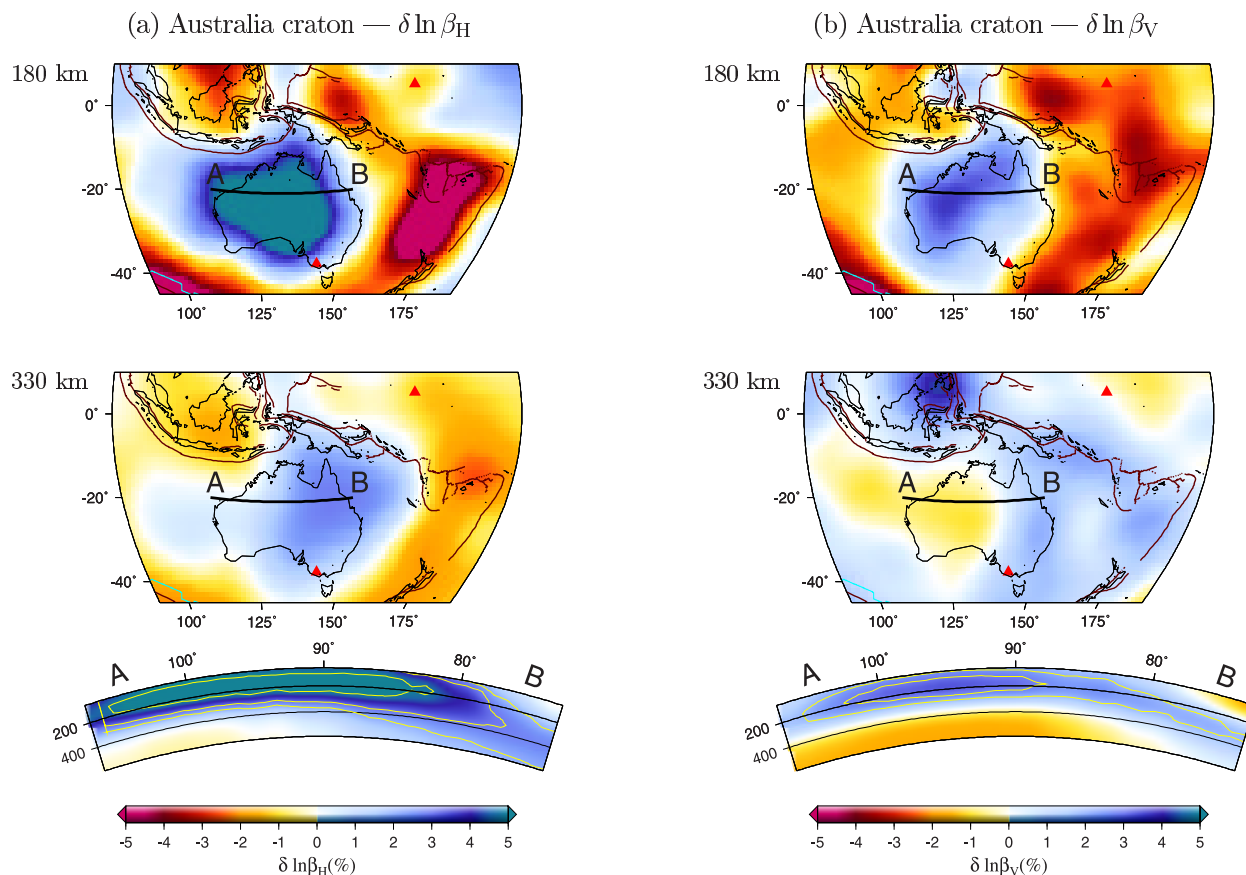
Figure 10. (a) Map views and AB depth cross-section of SH-velocity perturbations beneath the Australian craton. Red triangles indicate locations of hot spots, brown lines indicate plate boundaries. (b) SV-velocity perturbations. Map views are plotted at 180 km and 330 km; the yellow contours in the AB depth cross-sections indicate 2%, 3% and 5% of velocity perturbations. Velocity perturbations are with respect to a spherically symmetric reference Earth model, 1066A [*Gilbert and Dziewonski*, 1975].

roughness. We refer to a companion paper [*Zhou et al.*, 2005] for discussions on the tradeoff between the model roughness $\|\mathbf{Sm}\|$ and the data misfit χ^2 in solving the linear tomographic equation (8), for both finite-frequency tomography and ray-theoretical tomography.

4. Finite-Frequency Tomographic Model—FFSW1

4.1. Upper Mantle Shear-Wave Velocity and Anisotropy

[20] In this section we document the upper-mantle shear-wave velocity structure and radial anisotropy in our upper-mantle model, FFSW1, obtained by finite-frequency surface-wave tomography, using fundamental-mode phase-delay measurements with a longest period of 200 s.

[21] In Figure 8, global heterogeneity maps of shear-wave velocity $\delta \ln \beta_H$ and $\delta \ln \beta_V$, as well as radial anisotropy $\delta \ln \beta_H - \delta \ln \beta_V$ are plotted at depths of 120 km, 180 km, 250 km, 330 km, and 390 km. Velocity perturbations are with respect to the spherically symmetric Earth model 1066A [*Gilbert and Dziewonski*, 1975]. The long-wavelength features in the SH model do not vary greatly with depth, which reflects the similarity in the back projections of Love wave data at different frequencies (Figure 6). In the SH model, cratons exhibit fast anomalies and mid-ocean

ridges exhibit slow anomalies (Figure 8). The global average of the SH velocity is slightly faster than the reference model 1066A in the uppermost 220 km and is close to model 1066A at greater depths (Figure 9). In contrast, the global average of the SV velocity shows a strong deviation from 1066A at all depths. As a result, the global average of radial anisotropy is positive ($\beta_H > \beta_V$) in the uppermost 220 km and becomes negative ($\beta_H < \beta_V$) below 220 km (Figure 9). We emphasize that this polarity change in radial anisotropy is consistent with the Love-Rayleigh discrepancy observed at different frequencies (Figure 6). The positive radial anisotropy at depths between 120 and 220 km agrees well with the anisotropic Preliminary Reference Earth Model, PREM [*Dziewonski and Anderson*, 1981]; at shallower depths the magnitude of radial anisotropy in FFSW1 is smaller than PREM and PREM does not specify any anisotropy below 220 km (Figure 9). If we assume that radial anisotropy is induced by mantle flow through the mechanism of lattice preferred orientation, the transition from positive to negative anisotropy at about 220 km suggests that the lithosphere and asthenosphere are dominated by horizontal flow (or shearing), whereas below the asthenosphere, mantle flow is predominantly vertical.
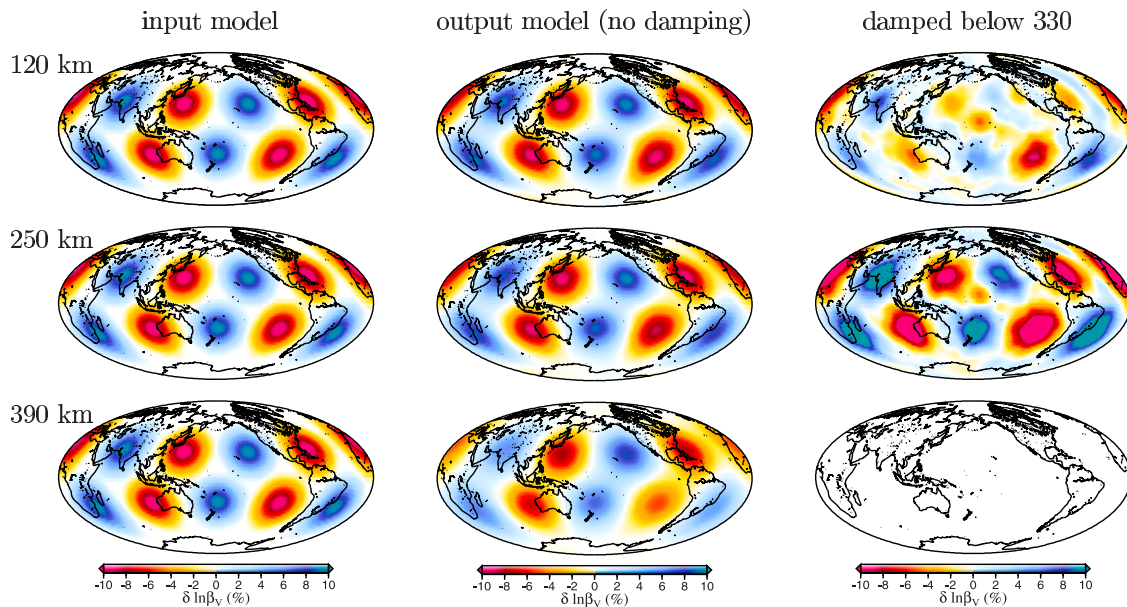
[22] This interpretation is based upon the assumption that radial anisotropy in the mantle is a result of lattice preferred orientation of mantle minerals at large strain. However,

(a) Love wave resolution — large anomaly test
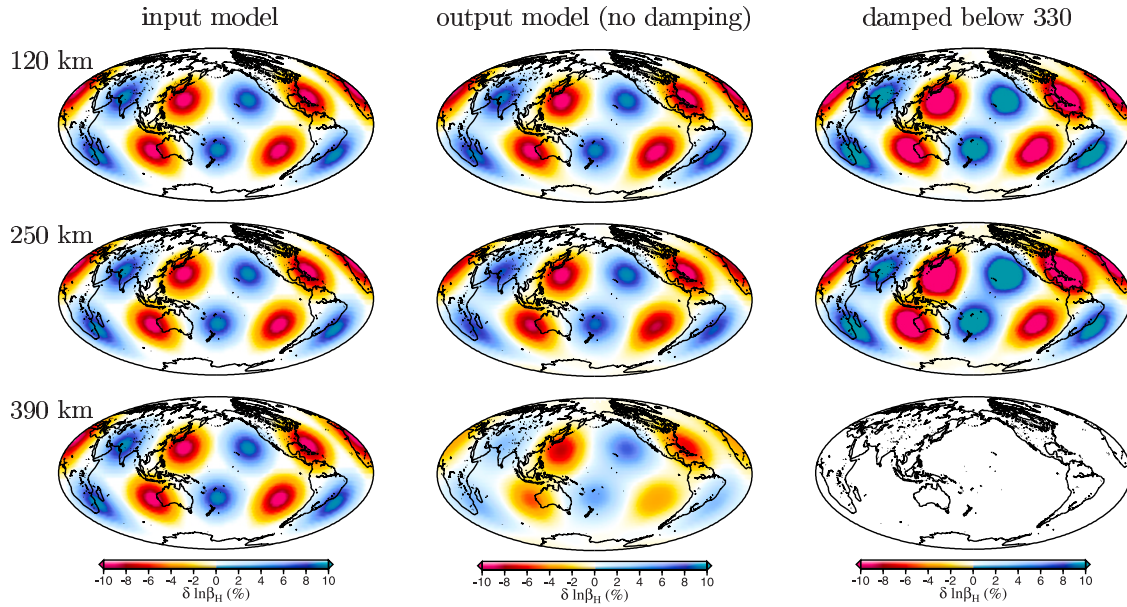
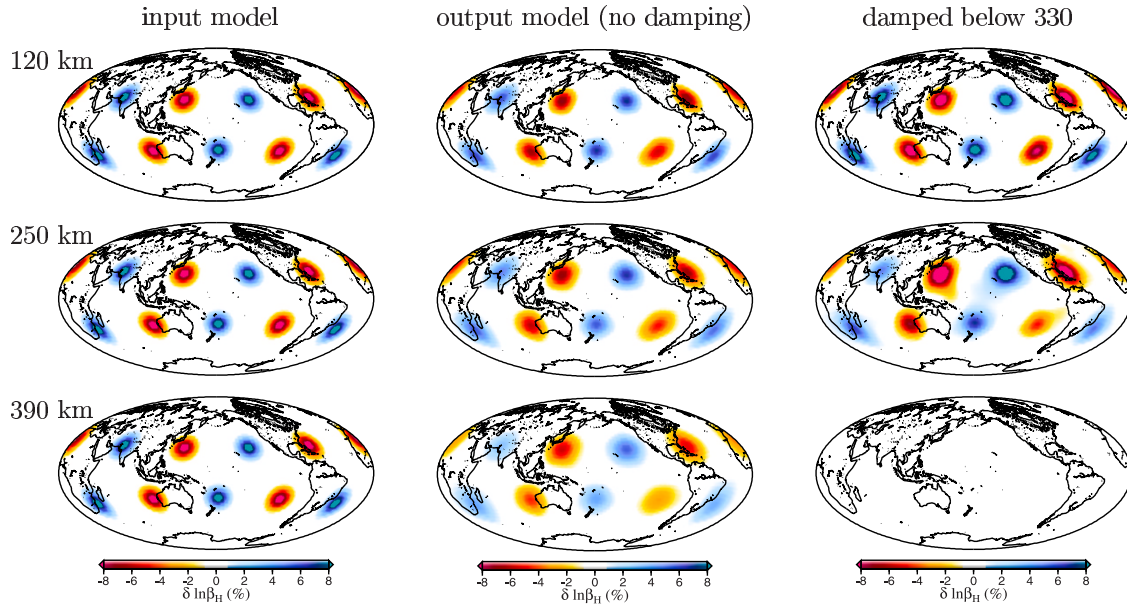## (b) Rayleigh wave resolution — large anomaly test

Figure 11. Resolution test using large isolated-anomaly synthetics for (a) Love waves and (b) Rayleigh waves. The input model consists of ten Gaussian anomalies, with a peak amplitude of 10%. The radius of each anomaly is about 20°; the size and amplitude of the anomalies do not vary with depth down to 580 km. All output models fit the synthetic data to $\chi^2/N = 1$. Synthetic phase delays are inverted with 50% (RMS) Gaussian noise. Models in the right panels are inverted with strong damping applied to structures at depths $\geq$330 km. The root-mean-square of the input and output models is plotted in Figure 13. The synthetic test shows that Love and Rayleigh waves used in this paper have significant sensitivity to structures below 330 km depth.

mantle rheology under the temperature and pressure conditions of the lower part of the upper mantle is not yet well understood. *Karato and Jung* [2003] suggested that pressure may have a strong influence on olivine dislocation creep and that therefore deformation in the lower part of the upper mantle may be dominated by diffusion creep, which, unlike dislocation creep, does not produce lattice preferred orientation. On the other hand, *Li et al.* [2003], based upon experimental studies at higher pressure, argued that dislocation creep is the dominant olivine deformation at high

(a) Love wave resolution — small anomaly test


(b) Rayleigh wave resolution — small anomaly test
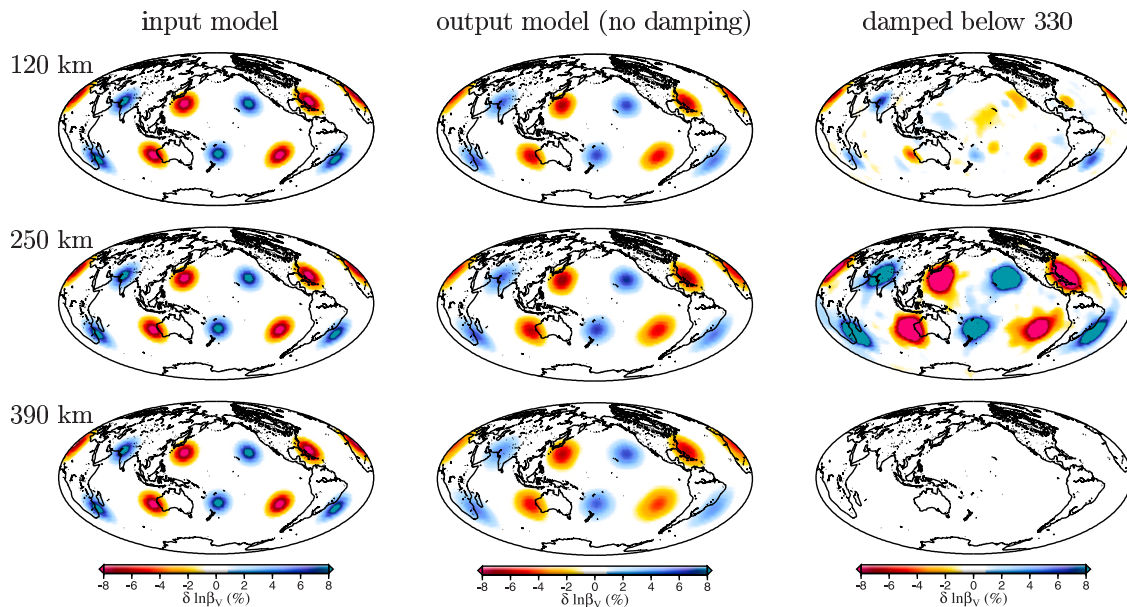
Figure 12. Same as Figure 11, except that the size of the anomaly is now about 10° in radius.

pressure, in which case lattice preferred orientation would be likely to develop in the entire upper mantle under large strain.

4.2. Cratons, Spreading Centers, and the Pacific

[23] SH and SV velocity anomalies are both correlated with surface tectonics at shallow depths, with fast anomalies beneath stable cratons such as the FennoScandian, Siberian, Canadian, Australian, and Antarctic shields and the Amazonian and northwest African cratons. SH velocities beneath cratons are generally faster than SV velocities, in agreement

with previous studies of radial anisotropy beneath continents [e.g., *Debayle and Kennett*, 2000; *Gung et al.*, 2003; *Gaherty*, 2004]. The craton signatures are strongest at 180 km depth, locally reaching 10% in our SH model and 6.5% in our SV model. The fast velocity anomaly beneath the Australia craton is plotted in Figure 10; the SH velocity is much faster than the SV velocity at shallow depths. In both the SH and SV models, the fast anomaly continues down at least to a depth of 250 km, rapidly fading away beneath this depth; however, the 2% fast velocity contours in both the SH and SV models
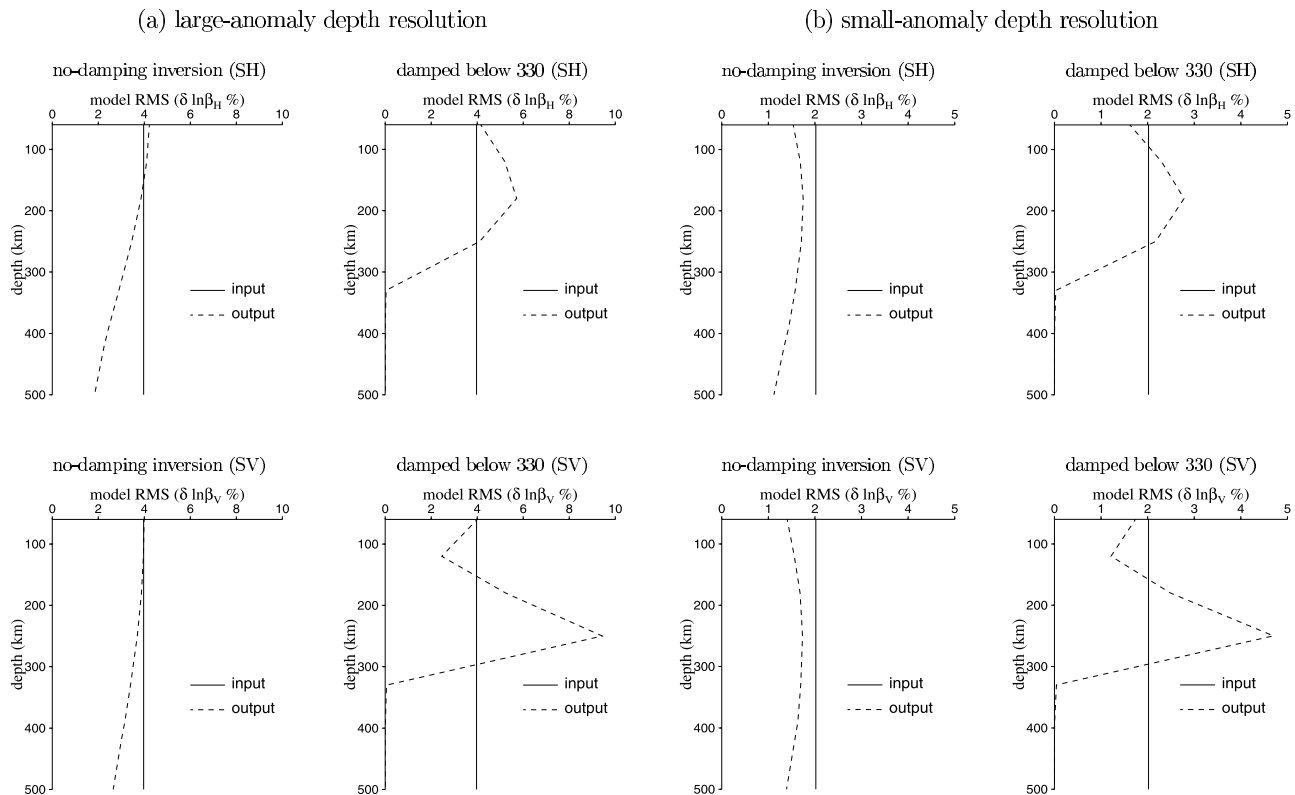
Figure 13. (a) Root-mean-square (RMS) depth profiles of the isolated-anomaly models in Figure 11; (b) RMS depth profiles of the models in Figure 12. In cases of the damped models, structures deeper than 330 km are damped to zero in the inversion, as a result, this introduces large errors in the output model at shallow depths. This confirms that both the Love-wave and Rayleigh-wave data used in this study have significant sensitivity to structures below 330 km. Rayleigh waves are more sensitive to deep structures ($\geq$330 km) than Love waves.

extend to about 330 km. Our estimate of the lower seismic boundary of the Australian craton is between 250 km and 330 km, in good agreement with estimates in this region based upon denser path coverage by *Simons et al.* [2002].

[24] Mid-ocean ridges show strong reductions in both the SH and SV velocity in the uppermost 200 km (Figure 8). At shallow depths $\leq$120 km, ridge anomalies show greater SV velocity reductions than SH so that the radial anisotropy is positive (indicative of horizontal flow). This global observation of ridge anomalies with positive radial anisotropy at shallow depths agrees with a previous regional study at the East Pacific Rise [*Webb and Forsyth*, 1998]. The slow SV anomalies beneath mid-ocean ridges become weaker at 180 km depth and become invisible beneath 250 km. In contrast, ridge anomalies extend to much greater depth in the SH model; in some regions the slow ridge anomalies are strong features continuing down to the transition zone. The globally averaged radial anisotropy changes from positive (horizontal flow) to negative (vertical flow) at about 220 km depth (Figure 9). This transition occurs at a shallower depth, between 120 km and 180 km, beneath mid-ocean ridges (Figure 8).

[25] In the asthenosphere at depths between 120 km and 250 km, most of the Pacific plate is dominated by positive radial anisotropy (Figure 8), with the SH velocity faster than model 1066A and the SV velocity slower than 1066A. The maximum radial anisotropy is centered west of Hawaii, in

agreement with the study of *Ekström and Dziewonski* [1998]. Hot spots are not clearly identified features at these depths. To the southeast of Hawaii, a strong anomaly with slow SV velocity is shown at these depths; this anomaly is very weak in the SH model. The Pacific "super plume" region appears as a distinct slow anomaly in the SH model at depths $\geq$330 km; at shallower depths this anomaly seems to be connected to the ridge anomaly at the Pacific-Nazca-Antarctic triple junction. The SH model displays slow anomalies in the South China Sea and the back-arcs associated with Pacific subduction, as well as beneath the Lau and Fiji Basin down to depths of 250 km.

[26] The magnitude of radial anisotropy shown in model FFSW1 is large; locally $\delta \ln \beta_H - \delta \ln \beta_V$ reaches 8% at a depth of 120 km and -7.8% at depths of 250 and 330 km, which is difficult to reconcile with current petrological models. In a pyrolitic model, mainly composed of olivine and orthopyroxene, the S-wave radial anisotropy may reach 8% only if crystals are perfectly aligned [*Maupin and Cara*, 1992]. S-wave radial anisotropy exceeding 8% has been reported in both global and regional studies [*Nataf et al.*, 1984; *Maupin and Cara*, 1992; *Debayle and Kennett*, 2000]. We note that the error in the radial anisotropy model is constructed from a difference and therefore is larger than in individual models for β_H and β_V, whose errors are influenced by the simplified assumption of radial anisotropy, which does not take into account any azimuthal depen-

(a) large-anomaly depth resolution — data fit
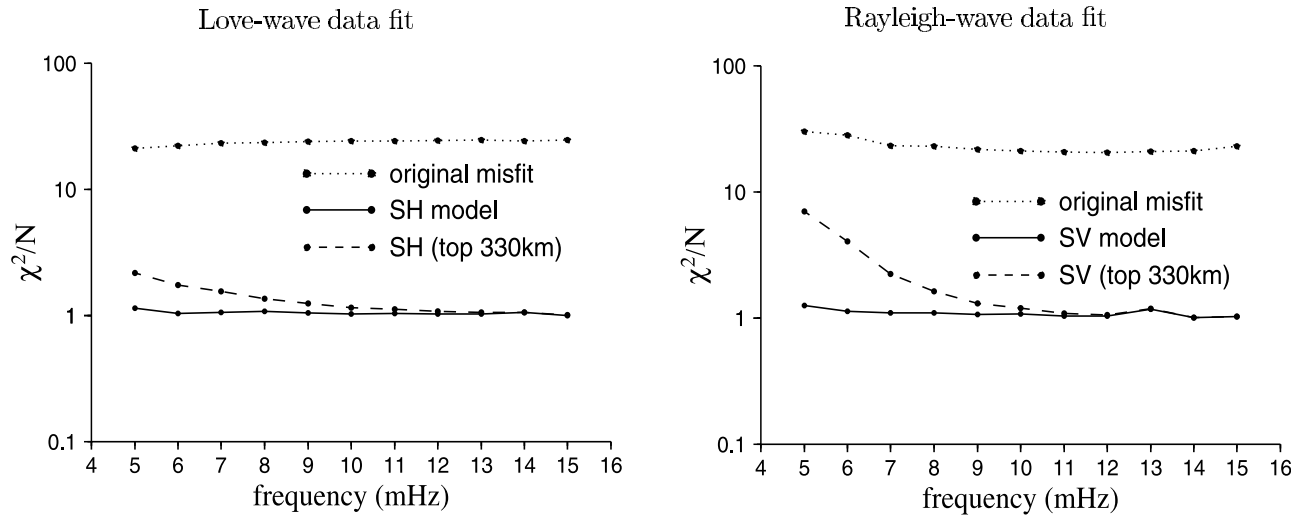
(b) small-anomaly depth resolution — data fit
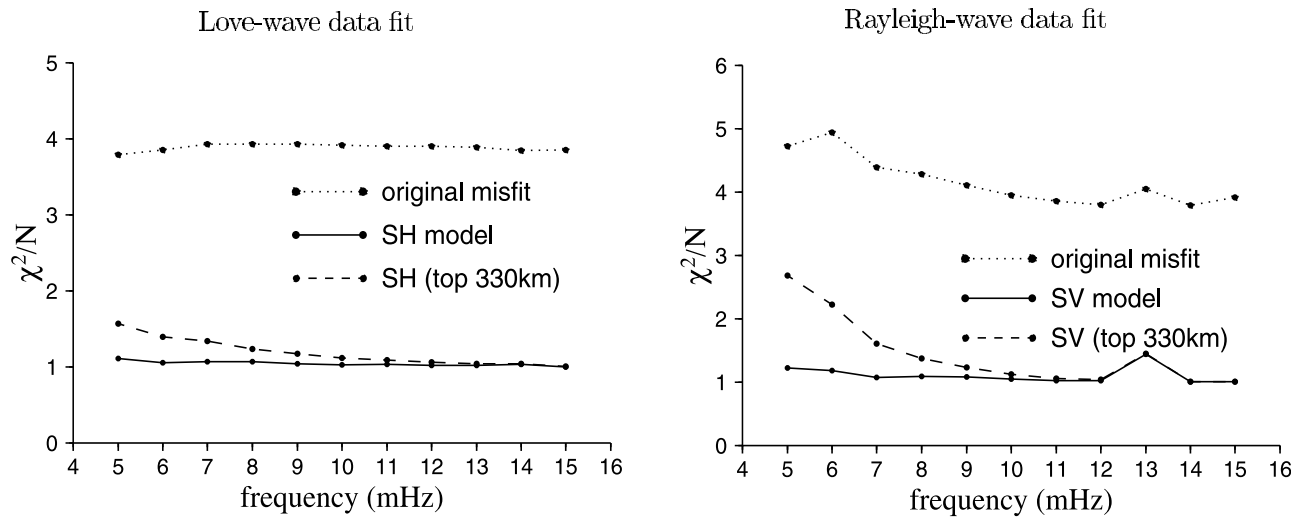
Figure 14. Love-wave and Rayleigh-wave data fit for (a) large and (b) small isolated-anomaly resolution tests. The χ^2/N at single frequencies is computed based on the isolated-anomaly models (left and middle columns) in Figures 11 and 12, respectively. The original data misfits (χ^2/N) are computed using the synthetic isolated-anomaly data (with Gaussian noise), and are plotted as dotted lines; the solid lines are the fitting curves of the output model; and the dashed lines are computed using only the uppermost 330 km of the output models.

dence of anisotropy. The observation that almost perfect alignment is required is therefore far from significant and in need of further confirmation.

5. Resolution Tests

[27] It is important to understand the geographic and depth resolution in seismic tomography, due to limited data and uneven path coverage. We test our model resolution at two length scales, using isolated-anomaly synthetics. The input anomalies consist of ten positive and negative Gauss-

ian balls, with a peak amplitude of ±10%. The size of the anomalies are about 20° (Figure 11) and 10° (Figure 12) in radius, respectively, representative of the characteristic length scales of mantle heterogeneities in model FFSW1. The size and amplitude of the anomalies do not vary with depth down to 580 km. Synthetic Love wave and Rayleigh wave phase delays are generated using the same path and wave train configurations as the global data set used in this study and inverted with 50% (RMS) Gaussian noise. The output models exhibit roughly Gaussian balls well recovered geographically in place, but with smaller amplitudes,
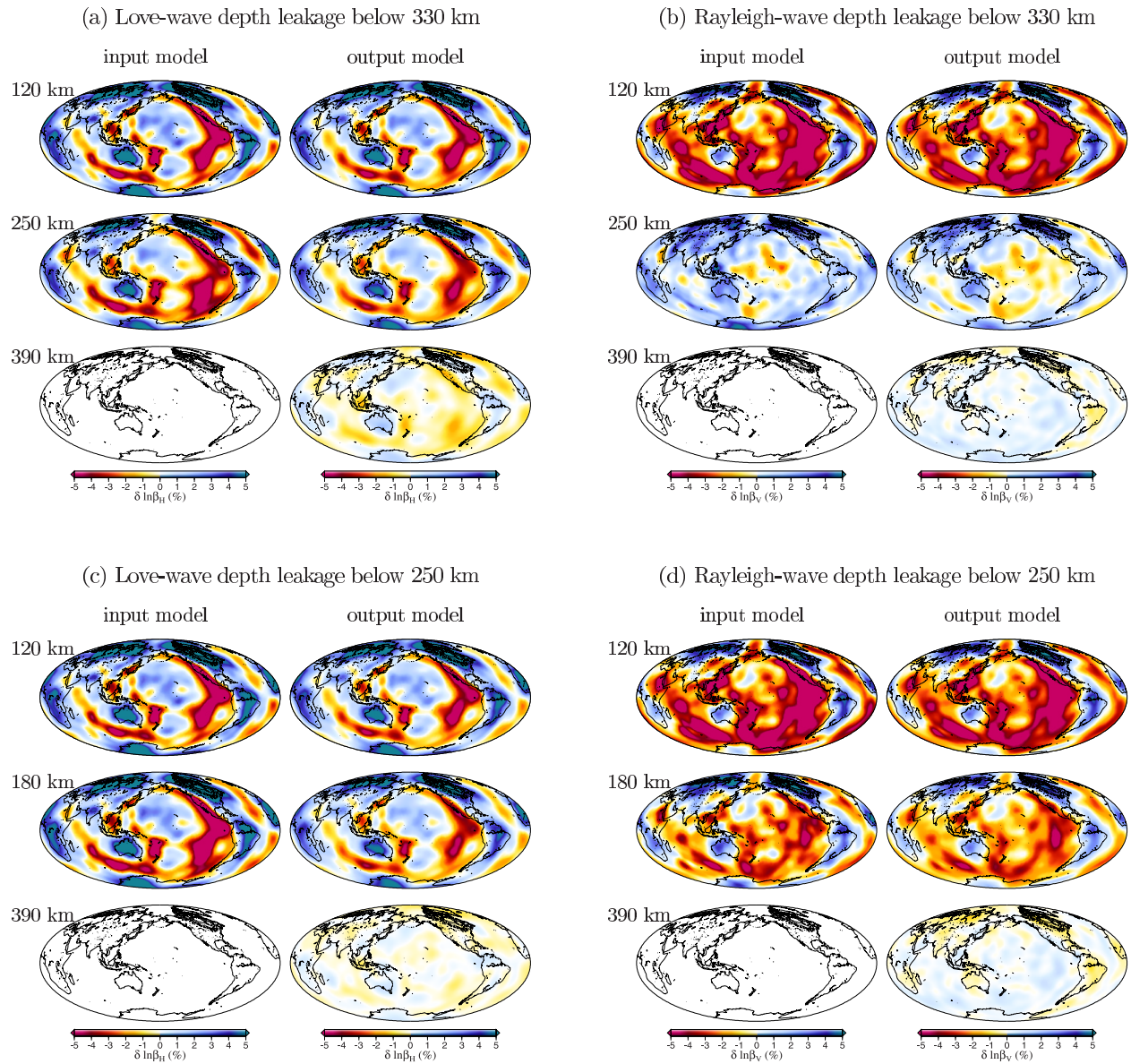
Figure 15. (a) and (b) Resolution tests of the downward depth leakage from the uppermost 330 km of the model. (c) and (d) Tests of the depth leakage from the uppermost 250 km. Synthetic phase delays are inverted with 50% (RMS) Gaussian noise, using the same smoothing parameter as in the real-data inversion. The input models in Figures 15a and 15b are identical to FFSW1 in the uppermost 250 km, with anomaly amplitude linearly decreasing to zero at 330 km. The input anomalies in Figures 15c and 15d are identical to FFSW1 in the top 180 km, with anomaly amplitude linearly decreasing to zero at 250 km. The RMS depth profiles of the input and output models are plotted in Figure 16. It is worth noting that depth leakage is inevitable due to limited path coverage, as well as random noise in the synthetic data.

mainly due to limited path coverage and random noise in the synthetic data. The recovered anomalies are especially weaker at greater depth due to reduced data sensitivity; the effect of smoothing is more pronounced for small velocity anomalies (Figures 11 and 12). To test the resolution at depths greater than 330 km, we perform additional inversions, with strong norm damping applied to structures below 330 km. The resulting SH and SV models with the same data fit ($\chi^2/N = 1$) show significant artifacts at shallow depths, especially in the SV model. The root-mean-square

(RMS) of the models in Figures 11 and 12 is plotted versus depth in Figure 13. The resolution tests show that mantle anomalies can be reasonably well resolved geographically and that the data set used in this study has significant sensitivity to upper-mantle structures deeper than 330 km.

[28] The sensitivity of our surface-wave data to mantle anomalies below 330 km can also be demonstrated by investigating the data misfit function, χ^2/N, for models with and without the deep structures included. In Figure 14, the original data misfits (dotted lines) are computed at single
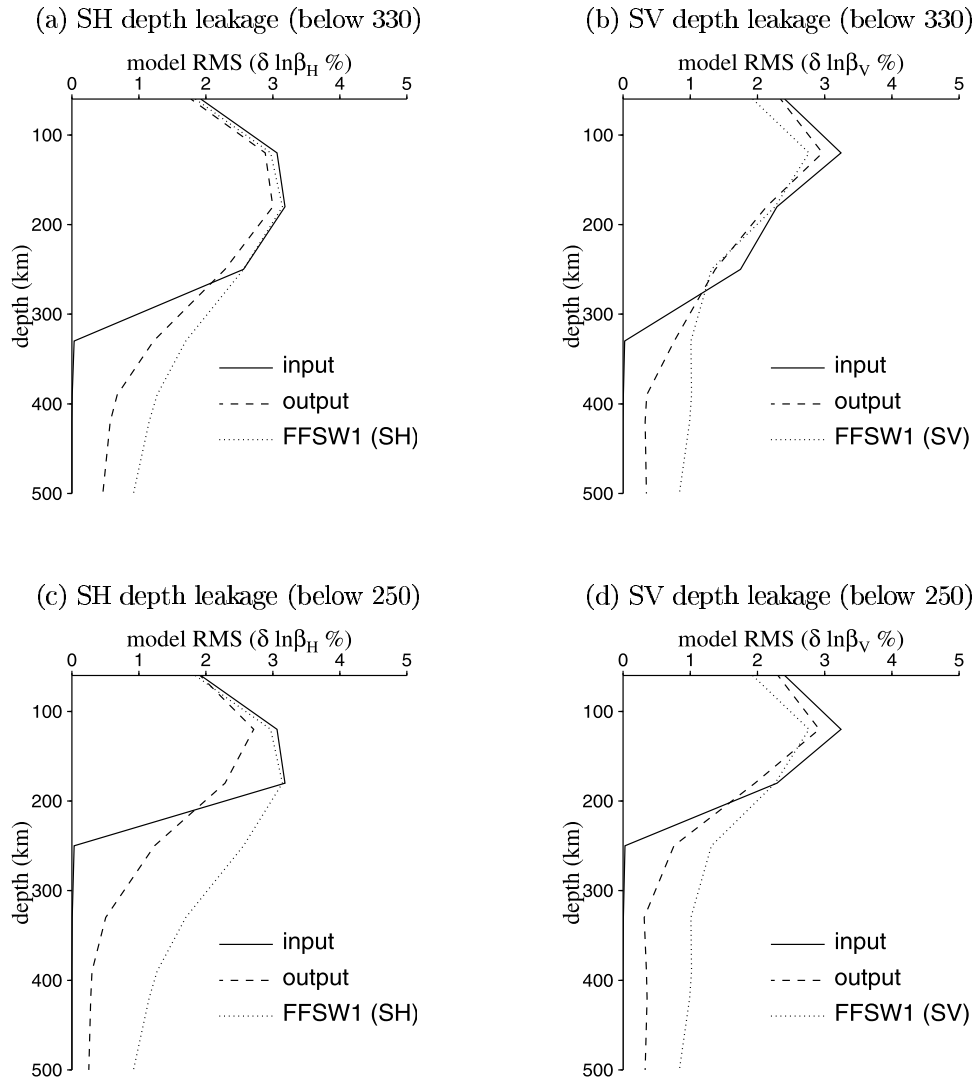
Figure 16. RMS depth profiles of the input (solid lines) and output (dashed lines) models in Figure 15. The RMS profiles of model FFSW1 (dotted lines) are plotted for reference. There is depth leakage in the output models due to limited path coverage and random noise in synthetic data; however, the RMS of model FFSW1 is well above the baseline of possible depth leakage.

frequencies for the isolated-anomaly synthetic data (with random noise), as well as for the output models with (solid lines) and without (dashed lines) the anomalies below 330 km included. The χ^2/N of the output models is close to 1 at all frequencies, as expected, and becomes substantially greater than 1 at frequencies lower than 10 mHz, for input models exhibiting only shallow anomalies ($\leq$330 km). The increases in χ^2 at low frequencies are more significant for Rayleigh waves. This confirms that Rayleigh waves have relatively stronger sensitivity to deep anomalies than Love waves do and that upper-mantle anomalies at depths greater than 330 km can be resolved, with damped amplitudes, by the low-frequency Love and Rayleigh waves used in this study.

[29] To understand the effects of possible depth leakage due to the smoothing applied in the inversion, we test the downward leakage problem using model FFSW1, truncated below two depths, 250 km and 330 km (Figure 15). Synthetic data are generated using the same path and wave

train configurations as the global data set used in this study and inverted with 50% random noise. The same smoothing parameters are used in the real-data inversion. The output models are plotted in Figure 15. These resolution tests show that it is unlikely that anomalies in the uppermost 250 km could leak down to a depth of 390 km and that there is small amount of leakage from anomalies in the depth range 250–330 km down to 390 km. The RMS versus depth of the input and output models is plotted in Figure 16. We should keep in mind that depth smoothing is inevitable due to limited data coverage and noise in the data. Therefore interpretations on the depth boundaries of weak anomalies should be made with great caution.

## 6. Mid-Ocean Ridge Anomalies: Shallow or Deep?

[30] The depth extent of mid-ocean ridges and the primary force that drives plate tectonics have been long-standing
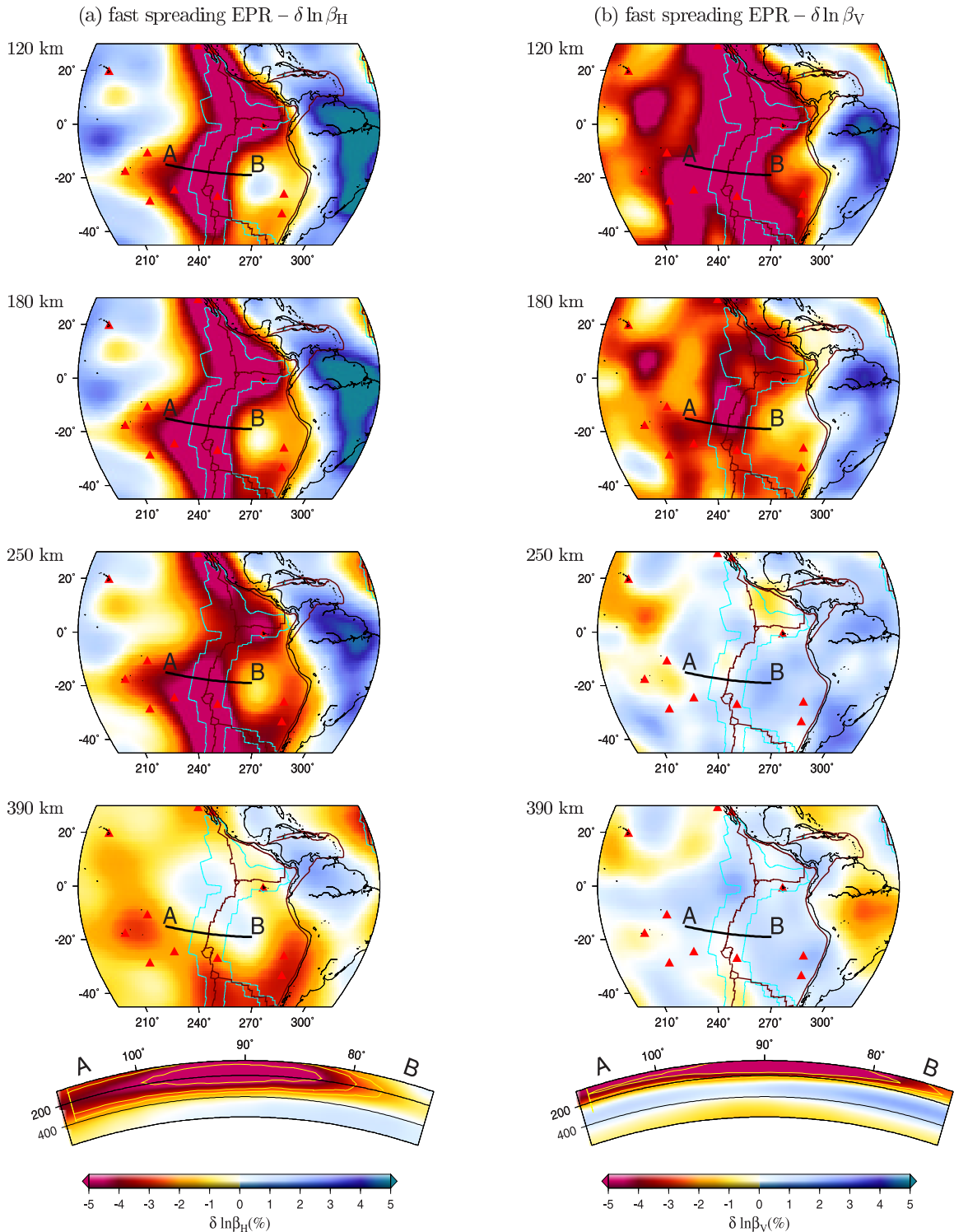
Figure 17. (a) Map views and AB depth cross-section of SH-velocity perturbations beneath a fast spreading center, the East Pacific Rise (EPR). (b) SV-velocity perturbations. Velocity perturbations are with respect to a reference Earth model, 1066A [*Gilbert and Dziewonski*, 1975]. The blue contours indicate sea-floor age of 10 million years, and the red triangles are hot spots. Contours in the depth cross-sections indicate −2%, −3%, and −5% of velocity perturbations. In the SV model (right), ridge anomalies are mostly confined to the uppermost 200 km; in the SH model (left), the lower boundary of the ridge anomalies is between 250 km and 330 km, except at the Pacific-Nazac-Antarctic triple junction, which may be affected by nearby hot spots.
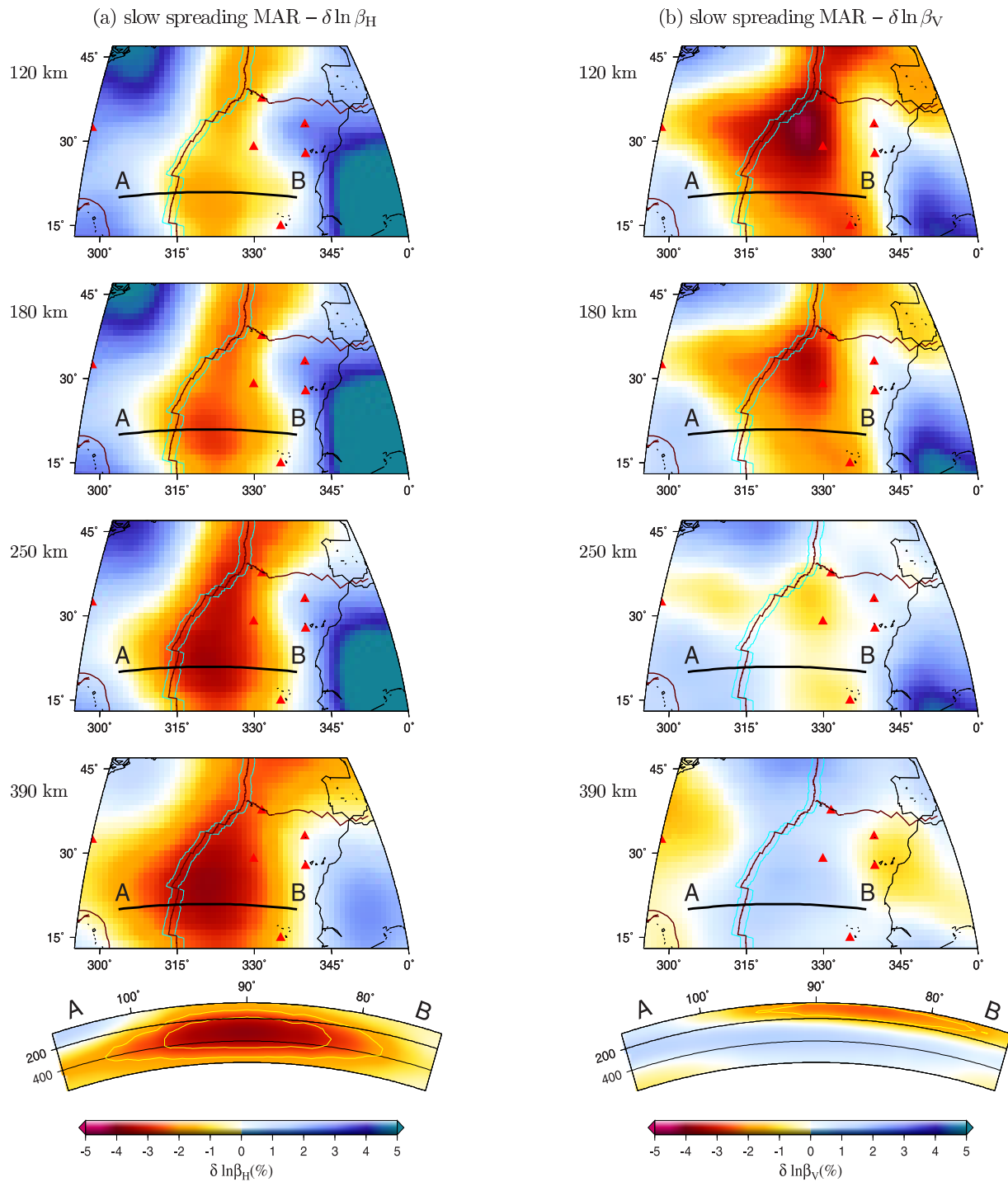
Figure 18. (a) Mapviews and AB depth cross-section of SH-velocity perturbations beneath a slow spreading center, the northern Mid-Atlantic Ridge (MAR). (b) SV-velocity perturbations. Velocity perturbations are with respect to a reference Earth model, 1066A [*Gilbert and Dziewonski*, 1975]. Contours in the depth cross-sections indicate −2% and −3% of velocity perturbations. In the SV model (right), ridge anomalies are mostly confined to the uppermost 200 km; in the SH model (left), ridge anomalies extend to much greater depth, at least to the top of the transition zone.

(a) Atlantic seafloor age

(b) $\delta \ln \beta_H$ at 390 km depth
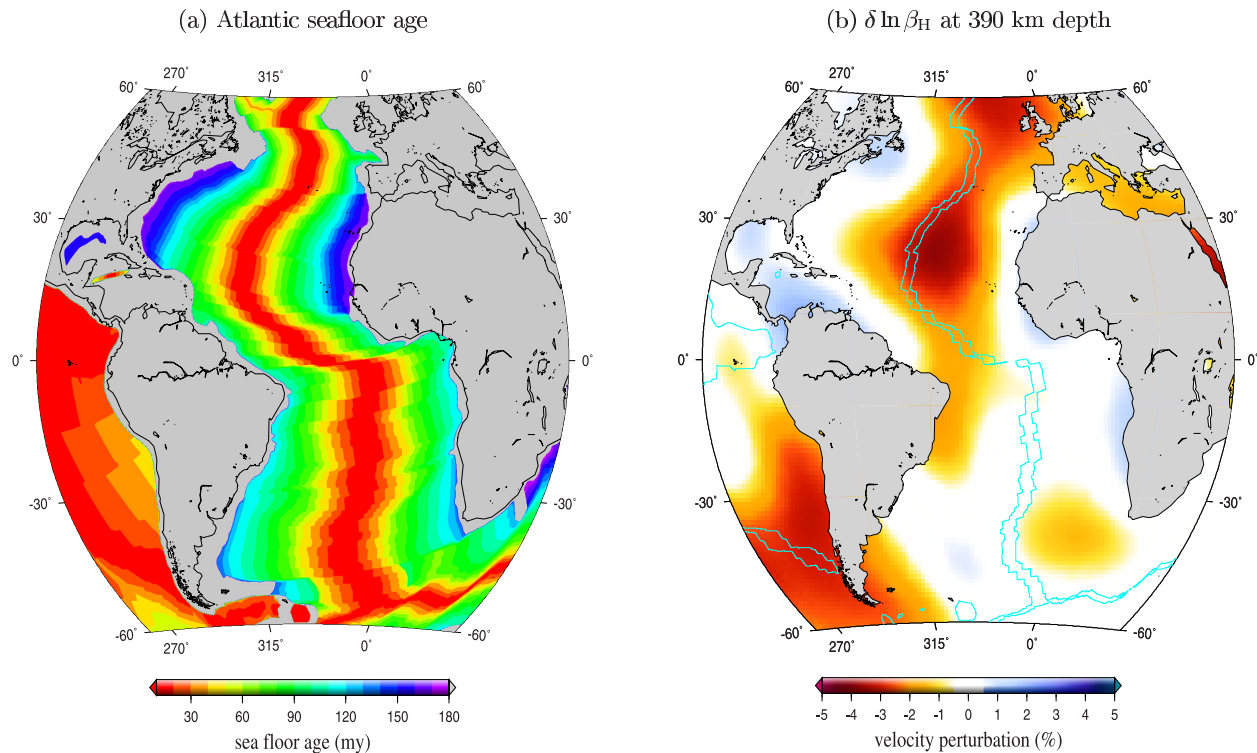
Figure 19. (a) Seafloor age in the Atlantic ocean basin. The oldest seafloor (blue-purple strips) is 180 million years old, off the coast of North America and Northwest Africa. (b) SH-velocity structure of the northern Mid-Atlantic Ridge (MAR) at 390 km depth, velocity perturbations are with respect to a reference Earth model, 1066A [*Gilbert and Dziewonski*, 1975]. It is worth noticing that the oldest sea floor is located at both sides of this ridge anomaly.

questions. It has been suggested on the basis of a torque balance estimate that the force of "slab pull" is an order of magnitude larger than "ridge push"; on the other hand, regions of seafloor with no connection to subduction are also spreading [e.g., *Forsyth and Uyeda*, 1975]. *Zhang and Tanimoto* [1992] initiated the debate on the depth extent of the seismically defined ridge anomaly. In their global tomographic model, mid-ocean ridges, regardless of their spreading rate, have shallow origins; therefore ridge anomalies are interpreted as purely passive adiabatic upwellings filling the gap between two separating plates. *Su et al.* [1992] argued that *Zhang and Tanimoto* [1992] underestimated both the magnitude and depth extent of mid-ocean ridges and proposed a global model in which most mid-ocean ridges extend continuously at least down to 300 km, and some ridge anomalies are as deep as 600 km, with possible connections to slow anomalies in the lower mantle. Regional seismic evidence from the MELT experiment indicates that seismic velocity reduction beneath the fast-spreading East Pacific Rise is concentrated at depths of about 100–150 km, with the bottom of the ridge anomaly possibly as deep as 200–300 km but not likely down to the transition zone [*Webb and Forsyth*, 1998; *Toomey et al.*, 1998; *Shen et al.*, 1998]. Ridge anomalies in regional surface-wave studies have so far been determined mainly using ray perturbation theory. In global tomography, the wavefront healing of surface waves has been accounted for using simplified two-dimensional, group-velocity sensitivity kernels by *Ritzwoller et al.* [2002], who point out that finite-frequency effects are most important in oceanic regions.

[31] In our model the fast spreading center along the East Pacific Rise shows a wide region of strong velocity reduction in both SH and SV at shallow depths (Figure 17). The ridge anomalies are mostly confined to the uppermost 200 km in the SV model, with a maximum velocity reduction at 120 km. The radial anisotropy $\beta_H > \beta_V$ (indicative of horizontal flow) at shallow depths $\leq$120 km agrees with a previous study by *Webb and Forsyth* [1998]. At greater depths, the SH velocity becomes slower than the SV velocity, indicating vertical flow. The lower boundary of the East-Pacific-Ridge anomaly in our model is between 250 km and 300 km, in agreement with a recent study by *Gu et al.* [2005], except at the Pacific-Nazca-Antarctic triple junction, where the ridge anomaly may not be distinguishable from nearby hot spots.

[32] The ridge anomaly beneath the northern Mid-Atlantic Ridge, a slow-spreading center, is characterized by an increasing reduction in SH velocity at least down to the transition zone (Figure 18). The −3% SH-velocity reduction contour extends well below 400 km. In the uppermost 180 km, the SV velocity is slower than the SH velocity; this positive radial anisotropy, indicative of horizontal flow at shallow depths, largely agrees with a regional study by *Silveira and Stutzmann* [2002]. Radial anisotropy below 180 km is negative (indicative of vertical flow), and the magnitude increases with depth down to 400 km (Figure 18). The center of the Mid-Atlantic Ridge anomaly at about 20°N is slightly to the west of the ridge. This might be correlated with the initial opening of the Atlantic ocean: with the North America plate drifting away from the Africa plate, the oldest
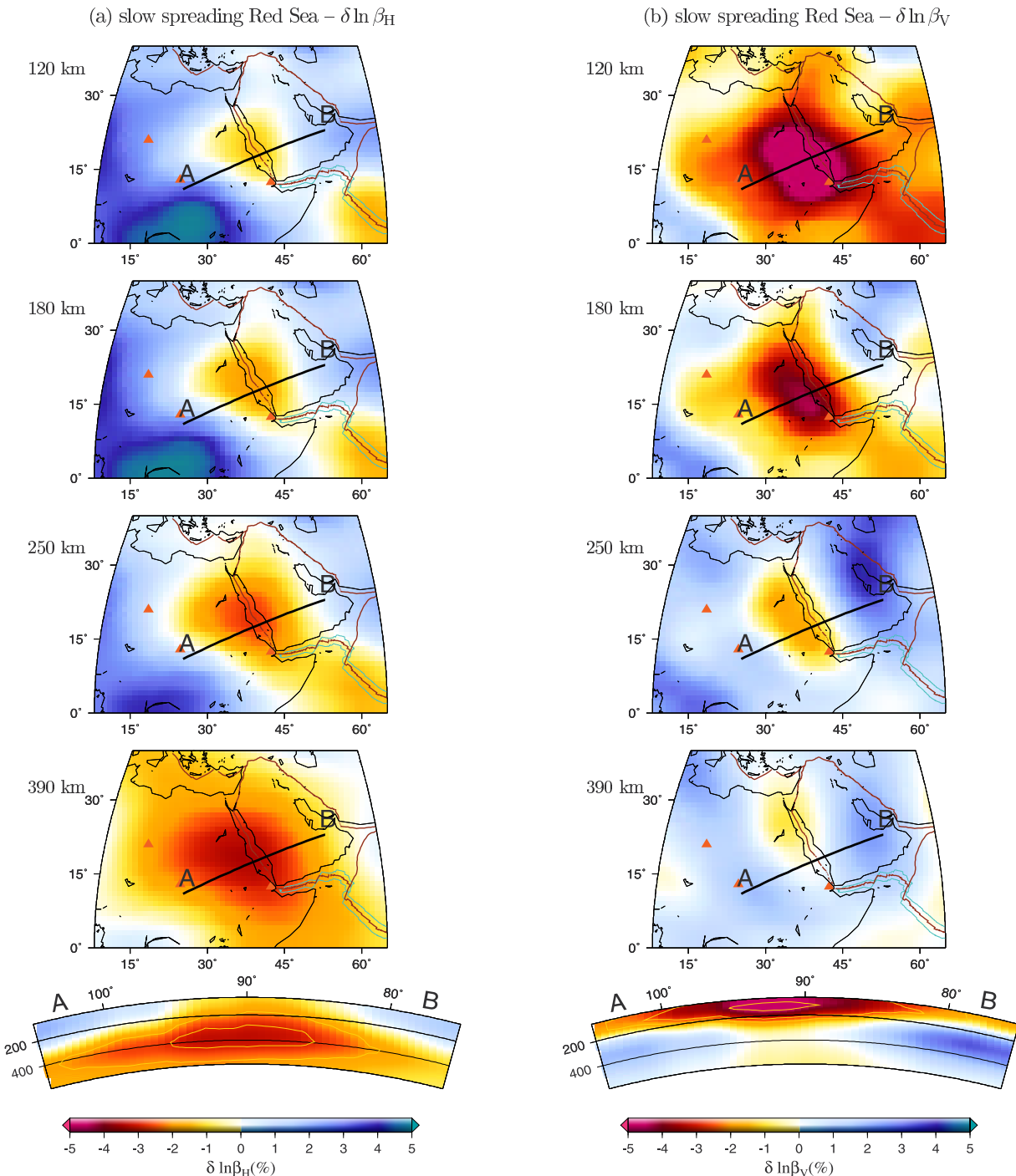
Figure 20. (a) Mapviews and AB depth cross-section of SH-velocity perturbations beneath a slow spreading center, the Red Sea. (b) SV-velocity perturbations. Velocity perturbations are with respect to a reference Earth model, 1066A [*Gilbert and Dziewonski*, 1975]. Contours in the depth cross-sections indicate −2% and −3% of velocity perturbations. In the SV model, ridge anomalies are mostly confined to the uppermost 200 km; in the SH model, ridge anomalies extend to much greater depth, at least to the top of the transition zone. Red triangles are hot spots. The Afar hot spot is near the southern end of the Red Sea.

seafloor in the Atlantic ocean basin is formed at both sides of the ridge anomaly, off the coast of North America and West Africa (Figure 19). This geographic correlation is consistent with the scenario that this deep slow anomaly provided the primary driving force for the initial opening of the Atlantic ocean 180 million years ago. This ridge anomaly is far away

from nearby hot spots, and the lower boundary of the anomaly cannot be determined using only the fundamental-mode surface waves used in this study. Therefore it is not clear whether this anomaly is connected to any deeper anomalies in the lower mantle; the age of this northern Mid-Atlantic anomaly is also an open question.
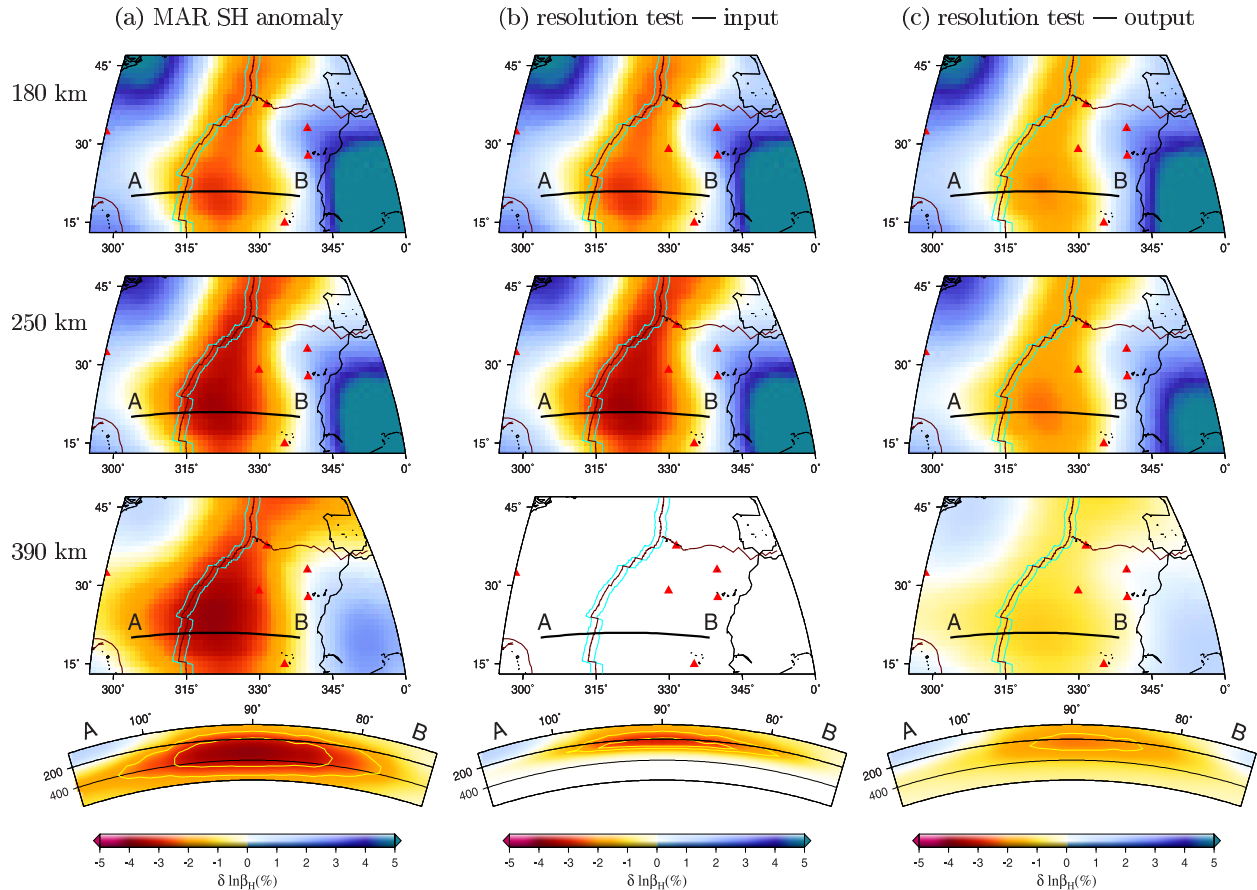
Figure 21. Depth resolution test of the Mid-Atlantic Ridge (MAR) anomaly. (a) The MAR SH anomaly in model FFSW1. (b) A test input SH model with velocities in the uppermost 250 km identical to model FFSW1, and linearly decreasing to zero at 330 km; the RMS of the input model is plotted in Figure 16a. (c) The output SH model, inverted with 50% (RMS) of Gaussian noise. Velocity perturbations are with respect to a reference Earth model, 1066A [*Gilbert and Dziewonski*, 1975]. There is depth smoothing due to limited path coverage and random noise in the synthetic data; however, the leakage is too small to explain the strong ridge anomaly at 390 km.

[33] A ridge anomaly with similar characteristics can be found beneath the slow-spreading Red Sea, a young spreading center at the beginning of the Wilson cycle (Figure 20). The center of the ridge anomaly is to the north of the Afar hot spot, but we cannot exclude the possibility that this ridge anomaly is connected to the deep mantle plume. The depth resolution tests of the two deep ridge anomalies, the Mid-Atlantic anomaly at 20° and the Red Sea anomaly, are plotted in Figures 21 and 22, respectively. There is a small amount of depth smearing due to noise in the data and limited path coverage; however, the deep anomaly in FFSW1 is far too strong to be explained by depth leakage. It is worth emphasizing that the ridge anomalies beneath these two slow-spreading centers become stronger with increasing depth and are therefore not likely to be a result of model smoothing.

[34] In summary, the ridge anomalies beneath fast and slow spreading centers are distinctly different from each other, which indicates that they may play different roles in the spreading of the sea floor. The strong and shallow ridge anomalies beneath the fast spreading center (>80 mm/yr) along the East Pacific Rise may be mainly passive upwell-ing in response to the separating Pacific and Nazca plates, with the main forces driving the seafloor spreading related to the subduction of the two plates. The anomalies beneath slow-spreading ridges exhibit only a modest reduction in the SH velocity at shallow depths; this suggests that the strength of shallow SH-velocity reduction beneath ridges depends upon the spreading rate. The deep ridge anomalies beneath the slow-spreading centers (<40 mm/yr) along the northern Mid-Atlantic and in the Red Sea may be indicative of active driving forces in the early stages of seafloor spreading.

7. Conclusions

[35] We report shear-wave velocity structure and radial anisotropy in the upper mantle, determined from finite-frequency fundamental-mode surface-wave tomography, based upon the background-spherical-Earth theory of *Zhou et al.* [2004]. Because wavefront healing effects are properly taken into account, finite-frequency surface-wave tomography improves the spatial resolution of small-scale mantle anomalies, especially at greater depth where the constraints are relatively weaker. The advantages of finite-frequency
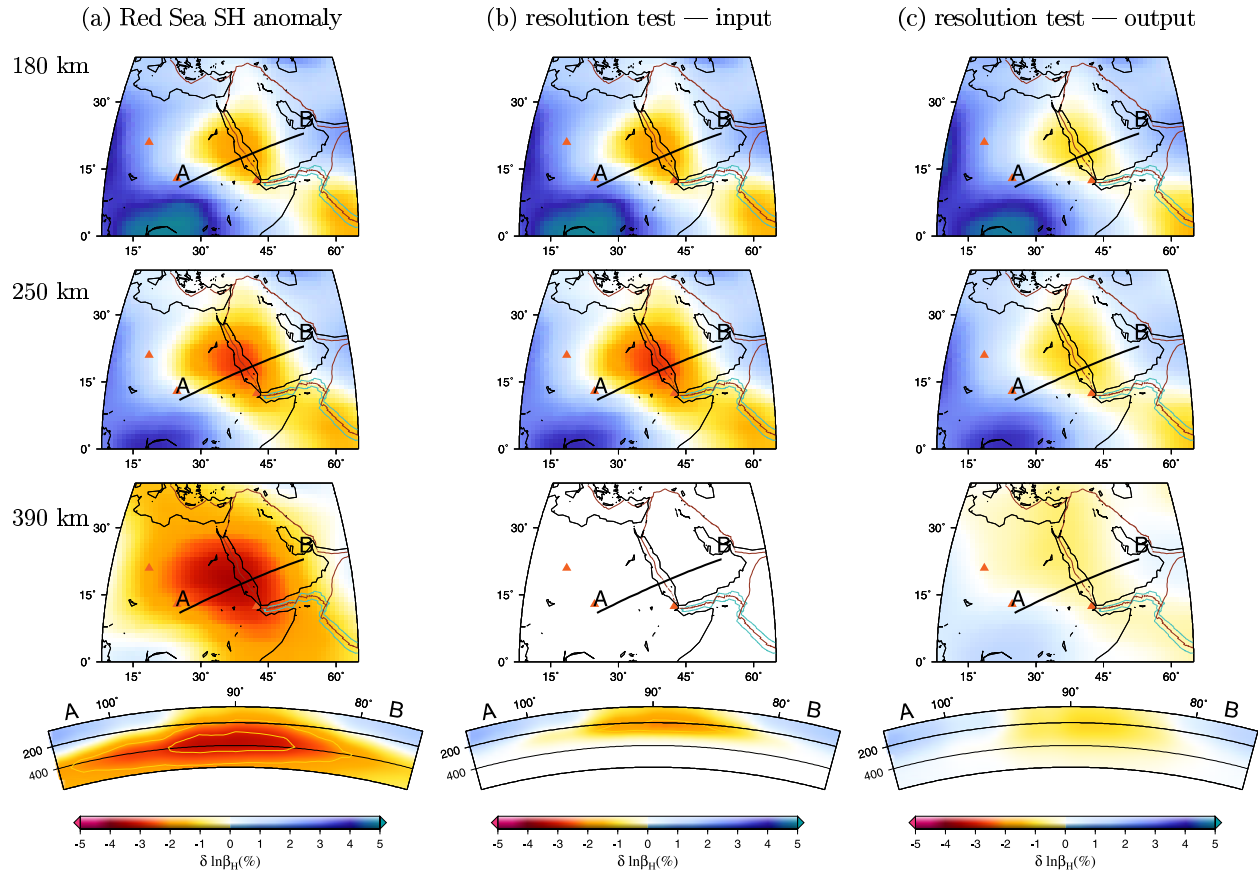
Figure 22. Depth resolution test of the Red Sea anomaly. (a) The Red Sea SH anomaly in model FFSW1. (b) A test input SH model with velocities in the uppermost 250 km identical to model FFSW1, and linearly decreasing with depth to zero at 330 km; the RMS of the input model is plotted in Figure 16a. (c) The output SH model, inverted with 50% (RMS) of Gaussian noise. Velocity perturbations are with respect to a reference Earth model, 1066A [*Gilbert and Dziewonski*, 1975]. There is smoothing induced depth smearing due to limited path coverage and random noise in the synthetic data, but the leakage is too small to explain the strong ridge anomaly at 390 km.

tomography over traditional ray-theoretical tomography have been documented by *Zhou et al.* [2005]. It is worth noting that the resolution of a tomographic model also depends upon the data path-coverage and that the finite-frequency upper-mantle model presented in this paper, FFSW1, is obtained using a small global data set of *Laske and Masters* [1996]. Finite-frequency sensitivity kernels should be equally beneficial in the inversion of larger global surface-wave data sets [e.g., *Trampert and Woodhouse*, 1995; *Ekström et al.*, 1997].

[36] To summarize, the globally averaged radial anisotropy is positive ($\beta_H > \beta_V$) in the uppermost 220 km of the mantle and becomes negative ($\beta_H < \beta_V$) below 220 km. This is consistent with lattice-preferred orientation anisotropy induced by predominantly horizontal mantle flow in the uppermost 220 km and predominantly vertical mantle flow beneath that. The transition from positive to negative radial anisotropy occurs at a shallower depth (between 120 and 180 km) beneath mid-ocean ridges and is not observed beneath continental cratons. The fast anomalies associated with continental cratons are characterized by strong positive radial anisotropy; these fast craton velocities are strongest at 180 km depth, where they locally reaches 10% in our SH model and 6.5% in our SV model. The old Pacific plate

show strong positive radial anisotropy (indicative of horizontal flow) in the uppermost 250 km, with maximum anisotropy west of Hawaii.

[37] The depth extent of the slow anomalies beneath mid-ocean ridges has been a long-standing question. In our model, ridge anomalies beneath fast and slow spreading centers are distinctly different. The fast spreading center along the East Pacific Rise is characterized by a strong ridge anomaly with the velocity reduction mostly confined to the uppermost 250 km. In contrast, the SH-velocity reductions beneath the slow-spreading centers along the northern Mid-Atlantic Ridge and in the Red Sea extend well below 400 km. This suggests that ridge anomalies associated with fast and slow spreading centers may play fundamentally different roles in the process of seafloor spreading. The fast-spreading East-Pacific-Rise anomaly may be a result of passive upwelling in response to separations of the Pacific and Nazca plate, whereas deep anomalies such as those beneath the slow-spreading Mid-Atlantic Ridge and the Red Sea may provide the primary driving force in the early stages of sea-floor spreading.

References

Aki, K., and K. Kaminuma (1963), Phase velocity of Love waves in Japan (part 1): Love waves from the Aleutian shock of March 1957, *Bull. Earthquake Res. Inst.*, *41*, 243–259.

Anderson, D. L. (1961), *Elastic wave propagation in layered anisotropic media*, *66*, 2953–2963.

Baumgardner, J. R., and P. O. Frederickson (1985), Icosahedral discretization of the two-sphere, *SIAM J. Numer. Anal.*, *22*, 1107–1115.

Crampin, S. (1975), Distinctive particle motion of surface waves as a diagnostic of anisotropy of layering, *Geophys. J. R. Astron. Soc.*, *40*, 177–186.

Debayle, E., and B. L. N. Kennett (2000), Anisotropy in the Australasian upper mantle from Love and Rayleigh waveform inversion, *Earth Planet. Sci. Lett.*, *184*, 339–351.

Dziewonski, A. M. (1971), Upper mantle models from "pure path" dipserssion data, *J. Geophys. Res.*, *76*, 2587–2601.

Dziewonski, A. M., and D. L. Anderson (1981), Preliminary reference Earth Model, *Phys. Earth Planet. Inter.*, *25*, 297–356.

Ekström, G., and A. M. Dziewonski (1998), The unique anisotropy of the Pacific upper mantle, *Nature*, *394*, 168–172.

Ekström, G., J. Tromp, and E. W. F. Larson (1997), Measurements and global models of surface wave propagation, *J. Geophys. Res.*, *102*, 8137–8157.

Forsyth, D. W. (1975), The early structural evolution and anisotropy of the oceanic upper mantle, *Geophys. J. R. Astron. Soc.*, *43*, 103–162.

Forsyth, D., and S. Uyeda (1975), On the relative importance of the driving forces of plate motion, *Geophys. J. R. Astron. Soc.*, *43*, 163–200.

Gaherty, J. B. (2004), A surface wave analysis of seismic anisotropy beneath eastern North America, *Geophys. J. Int.*, *158*, 1053–1066.

Gilbert, F., and A. M. Dziewonski (1975), An Application of Normal Mode Theory to the Retrieval of Structural Parameters and Source Mechanisms from Seismic Spectra, *Phil. Trans. R. Soc. London, Ser. A*, *278*, 187–269.

Gu, Y. J., A. L. Lerner-Lam, A. M. Dziewonski, and G. Ekström (2005), Seismic evidence for deep anisotropy beneath the East Pacific Rise, *Earth Planet. Sci. Lett.*, *232*, 259–272.

Gung, Y., M. Panning, and B. Romanowicz (2003), Global anisotropy and the thickness of continents, *Nature*, *422*, 707–711.

Karato, S., and H. Jung (2003), Effects of pressure on high-temperature dislocation creep in olivine, *Phil. Mag.*, *83*, 401–414.

Laske, G., and G. Masters (1996), Constraints on global phase velocity maps from long-period polarization data, *J. Geophys. Res.*, *101*, 16,059–16,075.

Li, L., P. Raterron, D. Weidner, and J. Chen (2003), Olivine flow mechanisms at 8 GPa, *Phys. Earth Planet. Inter.*, *138*, 113–129.

Love, A. E. H. (1927), *A Treatise on the Mathematical Theory of Elasticity*, Cambridge Univ. Press, New York.

Maupin, V., and M. Cara (1992), Love-Rayleigh wave incompatibility and possible deep upper mantle anisotropy in the Iberian Peninsula, *Pure Appl. Geophys.*, *138*, 430–444.

Montagner, J. P., and D. L. Anderson (1989), Petrological constraints on seismic anisotropy, *Phys. Earth Planet. Inter.*, *54*, 82–105.

Montagner, J. P., and N. Jobert (1988), Vectorial tomography II. Application to the Indian Ocean, *Geophys. J.*, *94*, 309–344.

Montagner, J. P., and H. C. Nataf (1986), A simple method for inverting the azimuthal anisotropy of surface waves, *J. Geophys. Res.*, *91*, 511–520.

Montagner, J. P., and T. Tanimoto (1990), Global anisotropy in the upper mantle inferred from the regionalization of phase velocities, *J. Geophys. Res.*, *95*, 4797–4819.

Nataf, H.-C., I. Nakanishi, and D. L. Anderson (1984), Anisotropy and shear-velocity heterogeneities in the upper mantle, *Geophys. Res. Lett.*, *11*, 109–112.

Paige, C. C., and M. A. Saunders (1982), LSQR: An algorithm for sparse linear equations and sparse lease squares, *ACM TOMS*, *8*, 43–71.

Ritzwoller, M. H., N. M. Shapiro, M. P. Barmin, and A. L. Levshin (2002), Global surface wave diffraction tomography, *J. Geophys. Res.*, *107*(B12), 2335, doi:10.1029/2002JB001777.

Shen, Y., A. F. Sheehan, K. G. Dueker, C. de Groot-Hedlin, and H. Gilbert (1998), Mantle discontinuity structure beneath the southern East Pacific Rise from P-to-S converted phases, *Nature*, *280*, 1232–1235.

Silveira, G., and E. Stutzmann (2002), Anisotropic tomography of the Atlantic Ocean, *Phys. Earth Planet. Inter.*, *132*, 237–248.

Simons, F. J., R. D. van der Hilst, J. P. Montagner, and A. Zielhuis (2002), Multimode Rayleigh wave inversion for heterogeneity and azimuthal anisotropy of the Australian upper mantle, *Geophys. J. Int.*, *151*, 738–754.

Smith, M. L., and F. A. Dahlen (1973), The azimuthal dependence of Love and Rayleigh wave propagation is a slightly anisotropic medium, *J. Geophys. Res.*, *78*, 3321–3333.

Su, W.-J., R. L. Woodward, and A. M. Dziewonski (1992), Deep origin of mid-ocean ridge seismic velocity anomalies, *Nature*, *360*, 149–152.

Tanimoto, T. (2004), The azimuthal dependence of surface wave polarization in a slightly anisotropic medium, *Geophys. J. Int.*, *156*, 73–78.

Tanimoto, T., and D. L. Anderson (1985), Lateral heterogeneity and azimuthal anisotropy of the upper mantle: Love and Rayleigh waves 100–250 s, *J. Geophys. Res.*, *90*, 1842–1858.

Toomey, D. R., W. S. D. Wilcock, S. C. Solomon, W. C. Hammond, and J. A. Orcutt (1998), Mantle seismic structure beneath the MELT region of the East Pacific Rise from P and S wave tomography, *Nature*, *280*, 1224–1227.

Trampert, J., and J. H. Woodhouse (1995), Global phase velocity maps of Love and Rayleigh waves between 40 and 150 s, *Geophys. J. Int.*, *122*, 675–690.

Webb, S. C., and D. W. Forsyth (1998), Structure of the upper mantle under the EPR from waveform inversion of regional events, *Nature*, *280*, 1227–1229.

Wessel, P., and W. H. F. Smith (1995), New version of the Generic Mapping Tools released, *Eos Trans. AGU*, *76*, 329.

Yoshizawa, K., and B. L. N. Kennett (2005), Sensitivity kernels for finite-frequency surface waves, *Geophys. J. Int.*, *162*, 910–926.

Zhang, Y.-S., and T. Tanimoto (1992), Ridges, hot spots and their interaction as observed in seismic velocity maps, *Nature*, *355*, 45–49.

Zhao, L., T. H. Jordan, K. B. Olsen, and P. Chen (2005), Frechet kernels for imaging the Los Angeles basin structure based on three-dimensional reference model, *Bull. Seismol. Soc. Am.*, *95*(6), 2066–2080.

Zhou, Y., F. A. Dahlen, and G. And Nolet (2004), Three-dimensional sensitivity kernels for surface wave observables, *Geophys. J. Int.*, *158*, 142–168.

Zhou, Y., F. A. Dahlen, G. Nolet, and G. Laske (2005), Finite-frequency effects in global surface-wave tomography, *Geophys. J. Int.*, *163*, 1087–1111.

————————
F. A. Dahlen, G. Nolet, and Y. Zhou, Department of Geosciences, Princeton University, Princeton, NJ 08544, USA. (fad@princeton.edu; nolet@princeton.edu; yingz@princeton.edu)

G. Laske, Institute of Geophysics and Planetary Physics, Scripps Institution of Oceanography, University of California, San Diego, La Jolla, CA 92093-0225, USA. (glaske@ucsd.edu)